INSTITUTO TECNOLOGICO Y DE ESTUDIOS
SUPERIORES DE MONTERREY
CAMPUS MONTERREY
PROGRAMA DE GRADUADOS EN ELECTRONICA,
COMPUTACION, INFORMACION Y COMUNICACIONES

PROPAGATION OF ROTATING INVARIANT OPTICAL FIELDS

T E S I S
PRESENTADA COMO REQUISITO PARCIAL
PARA OBTENER EL GRADO ACADEMICO DE:
MAESTRIA EN CIENCIAS EN INGENIERIA
ELECTRONICA CON ESPECIALIDAD EN SISTEMAS
ELECTRONICOS

POR
CARLOS LOPEZ MARISCAL

Monterrey, N. L., Noviembre de 2003

INSTITUTO TECNOLÓGICO Y DE ESTUDIOS SUPERIORES DE MONTERREY

CAMPUS MONTERREY

PROGRAMA DE GRADUADOS EN COMPUTACIÓN, INFORMACIÓN Y COMUNICACIONES

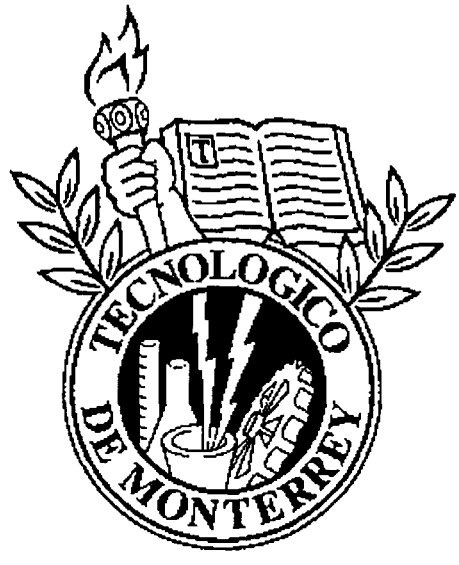

PROPAGATION OF ROTATING INVARIANT OPTICAL FIELDS

TESIS

PRESENTADA COMO REQUISITO PARCIAL PARA OBTENER EL GRADO ACADÉMICO DE:

MAESTRÍA EN CIENCIAS EN INGENIERÍA ELECTRÓNICA CON ESPECIALIDAD EN SISTEMAS ELECTRÓNICOS

POR:

CARLOS LÓPEZ MARISCAL

Monterrey, N.L., Noviembre de 2003

PROPAGATION OF ROTATING INVARIANT OPTICAL FIELDS

POR:

CARLOS LÓPEZ MARISCAL

TESIS

Presentada al Programa de Graduados en Electrónica, Computación, Información y Comunicaciones.

Este trabajo es requisito parcial para obtener el grado académico de Maestro en Ciencias en Ingeniería Electrónica con especialidad en Sistemas Electrónicos.

INSTITUTO TECNOLÓGICO Y DE ESTUDIOS SUPERIORES DE MONTERREY

Noviembre 2003

A Sirena.

"La tiene ahí para cuando quede tiempo,
para cuando aprenda a tocar melodías...
donde bailen los rayos rojos
y formen estrellas de cinco picos."

- Eugenia Garza

Acknowledgements

Many people contributed in a variety of ways to the successful termination of this work, some of them voluntarily, some inadvertently and some other with manifest reluctance. I would like to thank them all, regardless of their disposition and willingness.

I am particularly grateful to my thesis advisor and mentor, Dr. Julio César Gutiérrez Vega not only for his academic guidance, but also for his alarmingly constant availability, his seemingly unbounded patience and motivating example.

I am also indebted to Dr. Sabino Chávez Cerda, for many unorthodox yet insightful discussions. His almost heretical ability to synthesize complex situations into practical *gedanken* was key for the development of experimental techniques used in this work.

Special thanks to Dr. Hugo Alarcón Opazo for his time despite short notice. Also, to Dr. Carlos Hinojosa Espinosa, Dr. Daniel Jiménez Farías, Dr. Alfonso Serrano Heredia, and Dr. Rodolfo Rodríguez y Masegosa for their generous support regarding equipment and working areas.

Thanks to Magda Morales and Paty Vela for their help with cryptic administrative affairs and their friendship. I must also thank Ramiro Valdéz for doing the dirty work and yet remaining my friend.

Many thanks to Alberto Marino for useful discussion and for bibliographical references.

Friends not related to *Tec* played an important role in reminding me of aspects of life other than graduate school during this time. Thanks to Liz, Bere, Telina, Hernán, Dago, Carla, Ana Laura, Nadielly, Bryn, Brenda, Chelo, Mariamarta, Rosalinda, Ixchel, Thelma, Yadira, Mayra, Samantha, Esmeralda, Adriana, Sara and the fallen ones. Additionally, I wish to thank the occasional late-night visitors of the laboratory for serving as a bridge between experimental work and the outside world.

Thanks to my parents for nodding and to my sisters for frowning. Thanks to MFT for taking the time.

Thanks to Kena and to the forces that be.

Abstract

Rotating wavefields are characterized in order to describe the propagation of this class of propagation invariant optical fields (PIOFs). As the use of rotating wavefields for momentum transference in research applications has only recently been reported in the literature, experimental setups will aid in determining the feasibility of such applications of rotating wavefields in particular and PIOFs in general.

The present work is devoted to Bessel PIOFs and in particular, to a generation method based on interferometric techniques. Rotating Bessel wavefields are experimentally observed and characterized.

Contents

1 Introduction 1

2 Propagation Invariant Optical Fields 3
- 2.1 Theoretical background . . . 3
  - 2.1.1 Propagation invariant solutions of the wave equation . . . 4
  - 2.1.2 Additional considerations . . . 7
- 2.2 Bessel Beams . . . 7
  - 2.2.1 Generation of Bessel beams . . . 9
  - 2.2.2 Applications of Bessel beams . . . 12

3 Rotating Wavefields 13
- 3.1 Rotating scalar fields . . . 13
- 3.2 Rotating Bessel beams . . . 15
- 3.3 Interference of higher order Bessel beams . . . 17
  - 3.3.1 HOBBs and plane waves . . . 17
  - 3.3.2 HOBBs and spherical waves . . . 18
- 3.4 Generation of rotating wavefields . . . 20
- 3.5 Current experimentation with rotating wavefields . . . 21

4 Experimental Procedures 23
- 4.1 Experimental setup . . . 23
- 4.2 Description of experimental techniques . . . 26
  - 4.2.1 Photographic techniques . . . 27
  - 4.2.2 Lithographic techniques . . . 29
  - 4.2.3 Phase retardation methods . . . 32
  - 4.2.4 Assembly procedures . . . 35
  - 4.2.5 Setup integration . . . 35
- 4.3 Experimental results . . . 36
  - 4.3.1 Preliminary results . . . 36
  - 4.3.2 Results from interference . . . 38
  - 4.3.3 Invariance region measurements . . . 39
  - 4.3.4 Observation of rotating wavefields . . . 42

5 Conclusions **45**
5.1 Milestones 45
5.2 Difficulties 46
5.3 Forthcoming experimentation 46
5.4 Future work 47

References **47**

Vita **53**

Chapter 1

Introduction

Electromagnetic wavefields are found in everyday experience in both artificial and natural radiation sources, such as sun light, radio waves and artificial lighting, not to mention intensive radiation from exospheric sources [1]. Only as recently as the late 1960s have monochromatic light sources been available for the experimental study of light. Laser sources covering most of the electromagnetic spectrum are an ubiquitous and common tool in the laboratory nowadays. This availability allowed for the introduction and early experimental demonstration of one class of invariant solutions of the Helmholtz equation by Durnin [2, 3], although their mathematical foundations can be found much earlier in the literature [4].

The theoretical study of this class of fields has been intensive [5, 6, 7] and its consequences extended to a variety of technological fields in the search for applications that make use of the invariance characteristic [8, 9]. Numerous different techniques for construction of propagation invariant optical fields (PIOFs) have been developed ranging widely in their degree of technical complexity. The use of conical optics deserves a special mention amongst these since its use was reported as early as 1954 [10].

More recently, Gutierrez-Vega [11] has associated four fundamental classes of invariant optical fields in a one to one relation to the four cylindrical orthogonal coordinate systems by using group theory. Interestingly, these are the only possible classes of fundamental PIOFs.

Remarkable interest is set on the Bessel family of solutions because of the particular shape of the field, which attains an azimuthally symmetric intensity pattern while its phase gradually varies about the same coordinate. This feature has triggered several ideas in the atomic physics context relating the use of Bessel beams to confine and manipulate multiple particles in angular arrays by using only the radiation field and thus avoiding any physical contact with the microscopic elements of the array [12, 13, 14].

The main purpose of the present work is to experimentally demonstrate that one particular class of PIOFs, namely Bessel beams (BBs) can be generated by means of an interferometric optical setup. This method, which relies on the principles of coherent superposition of light, introduces an advantage over the traditional techniques for achieving this purpose. Bessel beams produced in this way are in principle not limited in their order in any way. The objective here is actually to obtain BBs of high

order, as opposed to the fundamental BB. This technique requires the use of a wavefront division interferometer as proposed by Gutierrez-Vega[15].

The experimental work of this thesis is devoted to produce an instance of gradual-phase beams for which diffractive optics are used. A significant part of the work herein focuses on the problem of generating the desired phase distribution on such diffractive optical elements.

The organization of this thesis is as follows. Chapter 2 is a general outline of the theoretical body of knowledge that has been developed regarding the invariant solutions of the wave equations, their most remarkable properties and a concise description of BBs. Some generation methods and applications of BBs are also presented.

Chapter 3 is intended to introduce the characteristics of rotating wavefields, in particular, those of higher-order BBs. Interference of rotating wavefields with plane and spherical waves is briefly analyzed and again, generation methods and current trends in their applications are outlined. Theoretical intensity distributions are provided in this and the previous chapter as examples of propagation invariant optical fields.

Experimental results constitute the central core of the present work, these are presented in Chapter 4 along with discussion of the experimental setup that was used to produce them and the techniques involved in its construction. Photographic sequences are provided for comparison with theoretical results from simulation.

Conclusions on this work are presented in Chapter 5, along with the difficulties and obstacles that arose during the development of the experimental work. An outlook on further work is also included.

Chapter 2

Propagation Invariant Optical Fields

This chapter comprises a physical description of one particular class of electromagnetic fields. Interest in this particular class of optical fields is due to an outstanding characteristic of its propagation. Namely, that the intensity distribution of the field remains unaffected as it propagates, hence the name: *propagation invariant optical fields* (PIOFs).

Firstly, the theoretical basis for the existence of such beams is presented in brief and the invariance property is explained in terms of such theory. A few examples of intensity distributions of different PIOFs are also shown. Next, a short discussion on some additional characteristics of PIOFs are given from selected research work done recently on the subject. The last part of this section is on the matter of Bessel beams, a specific subset of PIOFs with interesting characteristics of their own. The study of Bessel beams sets up the basis for the subsequent discussion of rotating wavefields, which is the main subject of the present work.

2.1 Theoretical background

Diffraction has an effect on the propagation of any electromagnetic field in either media or free space. This phenomenon, inherent to all undulatory transport in unbounded media or free space results in the dynamic redistribution of energy in the spatial configuration of wavefields as they propagate. The same holds true for fields associated to beams, even in spite of their apparently localized, narrow transverse spatial extent. An optical field distribution that is confined to a limited extent at an aperture, for instance, will undergo diffractive spreading as it propagates away from the aperture. A conventional measure of this effect on the field is given by the Rayleigh range, or the distance along propagation at which the transverse area of the beam field increases twofold. Correspondingly, the Rayleigh range is that distance at which the energy density associated to the beam decreases to half its initial value.

Particular consideration is given to a beam whose intensity profile in every cross

section is given by a Gaussian function, as this beam represents the fundamental mode of propagation or the first element of a complete set of solutions of the paraxial wave equation. The transversal radius or *spot size* w of a monochromatic Gaussian beam of wavelength λ, propagating in the z direction away from its origin is given by [16]:

$$w(z) = w_0 \left[1 + \left(\frac{z}{z_R}\right)^2\right], \tag{2.1}$$

where the Rayleigh range is given by [17]:

$$z_R = \frac{\pi w_0^2}{\lambda}, \tag{2.2}$$

and w_0 is the beam radius at $z = 0$. It is also customary to refer to $2w_o$ as the beam waist. Clearly, if the waist of a beam is arbitrarily reduced, its spot size will then spread in a shorter distance for a fixed wavelength.

2.1.1 Propagation invariant solutions of the wave equation

Durnin *et al.* [2, 3] pointed out, that a family of *diffraction-free* beams is physically possible. This class of beams would show no signs of diffractive divergence along propagation after an arbitrarily long distance. Such fields are also often termed diffractionless. At this point, it is worth mentioning that the indistinct use of the terms diffraction-free or nondiffractional is somewhat questionable, as it is actually diffraction itself the cause for the characteristic invariance of these fields. For this reason, *propagation invariant optical fields*, is a more suitable name.

Consider first the Helmholtz equation:

$$\left(\nabla^2 + k^2\right) E(\mathbf{r}) = 0, \tag{2.3}$$

where $k = \frac{2\pi}{\lambda}$ is the magnitud of the wavevector. Theoretically, a solution that complies with the condition:

$$\left|E\left(x, y, z > 0, t\right)\right|^2 = \left|E\left(x, y, 0, t\right)\right|^2, \tag{2.4}$$

would propagate indefinitely with an invariant intensity profile. Solutions that conform to this condition have been thoroughly studied [16, 3] after Whittaker [4]. In particular, an exact, nonsingular solution to Eq. (2.3) that satisfies the confition in Eq. (2.4)is given by:

$$E(x, y, z \geq 0, t) = e^{i(k_z z - \omega t)} \int_0^{2\pi} A(\varphi) \exp\left[ik_t \left(x\cos\varphi + y\sin\varphi\right)\right] d\varphi, \tag{2.5}$$

where $k_z^2 + k_t^2 = \left(\frac{2\pi}{\lambda}\right)^2 = k^2$, and, in the interpretation of the Fourier transform of E, $A(\varphi)$ is the complex angular spectrum of the field. Note that $|E(x, y, z, t)|$ does not depend on the coordinate z, so as to comply with Eq. (2.4).

In view of Eq. (2.5), it can be shown [6] that a sufficient condition for invariance under propagation is that the transverse frequency of the spectrum be given by the Dirac delta function; in other words, that the wave vectors that constitute the field E lie on the surface of a cone in K-space as shown in Fig. 2.1. The cone is characterized by the angle θ_0 of its envelope, in the relations: $k_z = k\cos\theta_o$, and $k_t = k\sin\theta_o$. This is evidently a consequence of Eq. (2.5) as this expression is the plane-wave decomposition of E. The wavevectors form a circular ring that lies at a constant value $|k_z|$ from the $k_z = 0$ plane. This geometrical locus is termed Montgomery's ring. The surface described in K-space by $K = |k|$ is usually referred to as McCutchen's sphere.

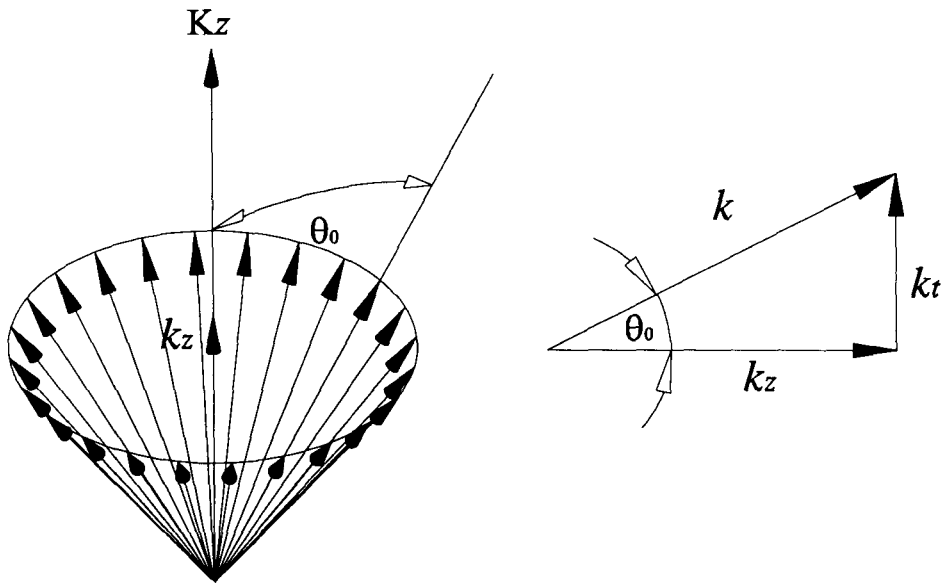

Figure 2.1. Angular spectrum in K-space for a PIOF. Wave vectors lie on the surface of a cone with semiangle θ_0.

In the simplest nontrivial case, $A(\varphi) = A$ is a nonzero real constant. Hence the left-hand-side of Eq. (2.5) is clearly the definition of the zeroth order Bessel function of the first kind $J_0(k_r\rho)$. The field is proportional to:

$$E(x,y,z \geq 0,t) = \frac{A}{2\pi}e^{i(k_z z-\omega t)}\int_0^{2\pi}\exp\left[ik_t\left(x\cos\varphi + y\sin\varphi\right)\right]d\varphi \tag{2.6}$$

$$E(x,y,z \geq 0,t) = \frac{A}{2\pi}e^{i(k_z z-\omega t)}J_0(k_t\rho), \tag{2.1}$$

with: $\rho^2 = x^2 + y^2$ for k_z real. In this case, a beam with transverse amplitude proportional to the fundamental Bessel function propagates *ad infinitum* with no degradation of its power distribution. The size of the central maximum is $2.405/k_t$, corresponding to the value of the first zero of $J_0(k_t\rho)$. In order to obtain this solution, an unbounded aperture was considered, resulting in infinite spatial extent of the Bessel field. Since this field is not square-integrable, it follows that such an ideal beam would carry an

infinite amount of energy at nearly constant *per annulus* energy density [18]. In practice though, this situation is not attainable, and the limited size of apertures results in finite field distributions that closely resemble the theoretical case. It has nevertheless been demonstrated, both theoretically and experimentally, that an actual truncated field shows propagation invariance along a finite distance. In this case, the field is not strictly propagation invariant, and thus it is said to be *pseudo-nondiffracting.* The invariance distance is determined by the experimental setup used, as will be seen below [19, 20].Note that since $A(\varphi)$ is an arbitrary complex function, there is an infinite number of solutions given by Eq. (2.5). A more detailed description of Bessel PIOFs is given in a subsequent section of the present work.

In general, for solutions in which $A(\varphi)$ depends on the angular coordinate, the field remains invariant, with a phase distribution that is not necessarily symmetric about the propagation axis [7]. Examples of the resulting invariant beams associated to a few particular angular spectra are shown in Figs. 2.2a-d. In particular, for Fig. 2.2c, the beam is the result of an angular spectrum given by: $se_n(\varphi, q)$, the odd angular Mathieu function of order n, where q is a parameter of ellipticity.

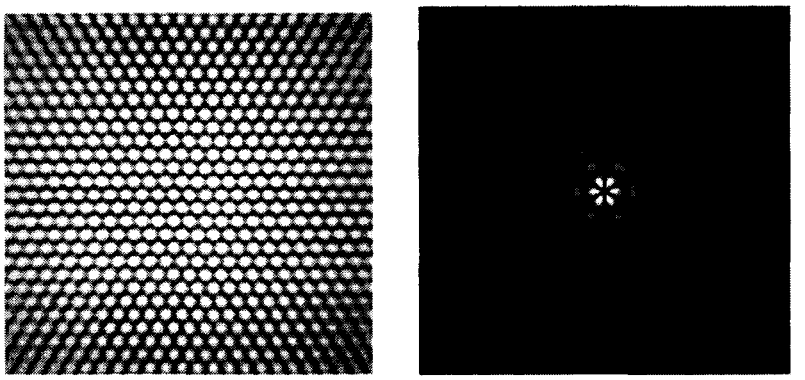

a. $A(\varphi) = \delta(e^{i3\varphi} - {r_0}^3)$. **b.** $A(\varphi) = \delta(r - r_0) \times \cos(3\varphi)$.

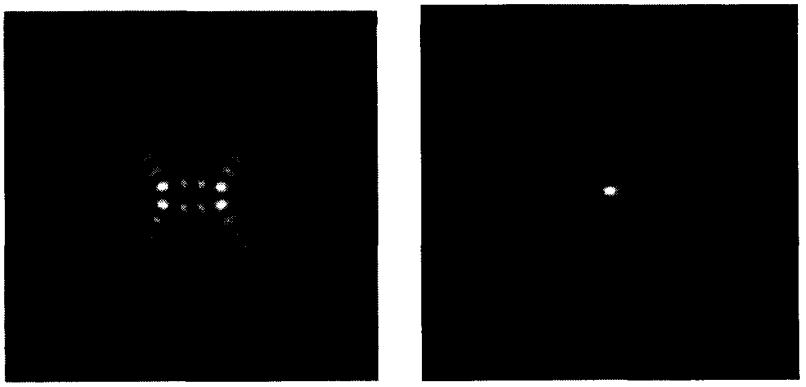

c. $A(\varphi) = \delta(r - r_0) \times se_3(\varphi)|_{q=20}$. **d.** $A(\varphi) = \dfrac{\delta(r - r_0)}{\cos\varphi}$.

Figures 2.2a-d. Various examples of PIOFs. a) Plane waves, b) Bessel-cosine beam, c) odd Mathieu beam, d) even parabolic beam.

2.1.2 Additional considerations

One remarkable property of PIOFs, aside from its invariance upon propagation is self-reconstruction. That is, if a PIOF is obstructed by an opaque obstacle in its path, diffraction reshapes its intensity profile accordingly, but after some distance beyond the obstacle the original field distribution is reconstructed. This phenomenon has been explained in terms of Babinet's principle [6], and in terms of counter-travelling waves within the region of invariance [21]. It is important to note that even though pseudo nondiffractional beams do show transverse intensity pattern invariance over a finite distance, the intensity value at a single point ρ_1 undergoes oscillations at different values of z within the invariance region.

Due to the conical distribution of the plane waves composing a PIOF, it can be found that the axial intensity shows interesting properties when an invariant beam is focused. In essence, an additional apparent focus can be seen to form near the actual focal plane. This seemingly anomalous behavior has been proven to be consequential of the spatial frequencies that constitute the PIOF and is not related to the aperture-induced focal shift or any other geometric-optics effect [22]. Interestingly, one can adjust the parameters of the beam in order to attain a second intense focal plane with a given magnification.

It can also be seen from Eq. (2.5) that a superposition of n invariant fields with frequencies $\{\omega_n\}$ subject to:

$$\omega_i \cos\theta_{0i} = \omega_{i+1} \cos\theta_{0i+1}, \text{ and} \tag{2.7a}$$

$$\omega_i (\sin\theta_{0i} - 1) = \omega_{i+1} (\sin\theta_{0i+1} - 1) \text{ for all } i \leq n, \tag{2.7b}$$

is also an invariant field, in the sense that the average intensity remains constant at a given point r with different values of z. Thus a field needs not be monochromatic in order to present invariance. Additionally, reports of partially coherent invariant fields can be readily found in the literature [5, 23, 24]. Experiments related to such fields are in agreement with the theoretical results for their fully coherent counterpart.

Nondiffracting beams have been extensively studied and classified according to their behavior upon propagation [25]. A subclass of PIOFs will be described in a later section as the main subject of the present work.

2.2 Bessel Beams

In general, if $A(\varphi) = e^{im\varphi}$,with m an integer, the field amplitude solution is proportional to the m-th order Bessel function of the first kind, whereas the phase modulation persists unperturbed in the PIOF. That is:

$$E(x, y, z \geq 0, t) = e^{i(k_z z - \omega t)} \int_0^{2\pi} e^{im\varphi} \exp\left[ik_t (x\cos\varphi + y\sin\varphi)\right] d\varphi \tag{2.8}$$

$$E(x, y, z \geq 0, t) = J_m(k_t\rho) e^{im\varphi} e^{i(k_z z - \omega t)} \tag{2.9}$$

Because of the narrow, intense central region of the fundamental Bessel beam and the self-reconstruction feature, interest was promptly centered around the seminal work of Durnin due mainly to the potential uses of nondiffracting beams in different power-carrying and precision alignment applications.

Higher order Bessel beams (HOBBs), unlike the fundamental Bessel wavefield, show low-intensity extended regions with minima at their axes origin. The relative extent of this region increases with the order of the beam. In Fig. 2.3 intensity profiles for different Bessel wavefields are shown.

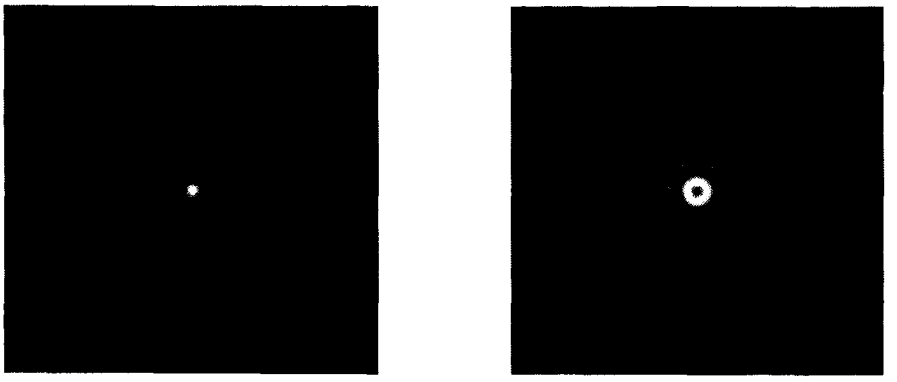

a. $I(\rho) = {J_0}^2(k_t\rho)$. **b.** $I(\rho) = {J_1}^2(k_t\rho)$.

c. $I(\rho) = {J_5}^2(k_t\rho)$. **d.** $I(\rho) = {J_{11}}^2(k_t\rho)$.

Figures 2.3a-d. Intensity profiles for Bessel wavefields of orders $m = 0$, 1, 5 and 11 respectively. Note that the spatial extent of the central minima increases with the order after the fundamental wavefield.

Likewise, an assortment of different methods for the generation of nondiffractional beams were thoroughly researched. The main challenge in generating a Bessel field distribution lies not only in creating the conical spectrum of wavevectors, but also in effectively managing to modulate the amplitude of the field in the angular coordinate. In principle, the most straightforward method to create the conical set of wavevectors involves the use of a conical optical element, namely, an axicon[1]. This procedure

[1] Conical elements have been widely used in the design of unstable resonators. Currently, there are several variations to the regular conical lens, such as the toroidal and radial axicons, the W-axicon and the *reflaxicon*, short for "reflective axicon" [26, Ch. 23].

was originally proposed by McLeod [10] although not in the context of propagation invariance. The complex amplitude modulation however, represents a challenge that is open to many options, most of which are considerably complicated, or expensive, to implement.

Regarding its intensity transverse profile, Bessel beams resemble concentric light cylinders with a symmetric power density that gradually decreases with distance away from the propagation axis. This singular mark has motivated extensive research regarding the generation and propagation of Bessel beams.

2.2.1 Generation of Bessel beams

Although axicons are frequently used in optical systems, mostly in order to achieve extended regions of field depth, their use in practice is limited by the difficulties involved in their fabrication. Fig. 2.4 shows the rays involved when a plane wave impinges on the plane surface of an axicon with index of refraction n , radius a and base angle α. The incident wavefront experiences a shift in phase that decreases with the radial coordinate away from the optical axis, thus resulting in two conical waves, one that converges and one that diverges from the apex of the axicon. By Snell's law, rays parallel to the optical axis are deviated towards the vivinity of the optical axis after the axicon and then interfere within a longitudinal region of limited extent:

$$Z_{MAX} = \frac{a}{\sin\theta} \tag{2.10}$$

along the propagation coordinate. After this distance, the paraxial region is obscured by the expanding geometrical shadow once the resulting conical wavefronts propagate away. For small values of α [27],

$$Z_{MAX} \simeq a\left(\frac{n-1}{\alpha}\right). \tag{2.11}$$

The distance Z_{MAX} is thus said to be the length of the invariance region. Typically, α is a few degrees so that long regions of invariance can be realized for practical purposes. Note that an axicon is capable of creating a good approximation to a fundamental Bessel beam only, since no phase modulation is introduced in the angular coordinate. An additional phase plate can be introduced before the axicon to generate higher-order Bessel distributions. Recently, Laguerre-Gauss (LG) beams of angular order l and radial index p have successfully been used to approximate l-th order Bessel beams taking advantage of the azimuthal phase variation $\exp(il\varphi)$ associated to LG beams [28]. Additionally, the profile of the axicon can be modified away from its linear phase dependency in order to induce a magnification of the output image. The fabrication of quality axicons involves technical difficulties and hence high costs, which constitute the main disadvantages for this experimental arrangement.

In the experimental verification of Durnin's work, an annular ring mask was placed in the back focal plane of a positive lens in order to generate a fundamental Bessel beam [2]. Here, the fact that the Fourier transform of a thin ring is indeed a Bessel

function [29] was used advantageously. The experiment is simple in principle: a plane wave is now incident in a slide portraying a thin translucid ring of radius a. A positive lens of radius R and focal distance f operates the Fourier transform on the emerging field resulting in two conical waves that interfere in a region of invariance. In this case, geometrical optics approximates the invariance region to:

$$Z_{MAX} = f\frac{R}{a} \tag{2.12}$$

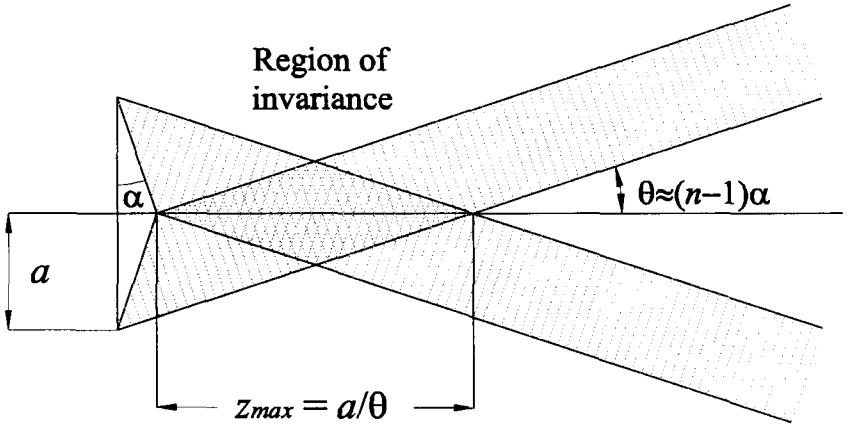

Figure 2.4. Axicon experimental setup.

Durnin's setup is shown in Fig. 2.5. Using photoreduction techniques allows for inexpensive slides with ring radii of a few hundred microns. Additionally, a large, long focal distance Fourier lens is typically available so that invariance distances of the order of 10^1 meters are easily realizable. The efficiency of this simple setup is rather limited by the annular aperture.

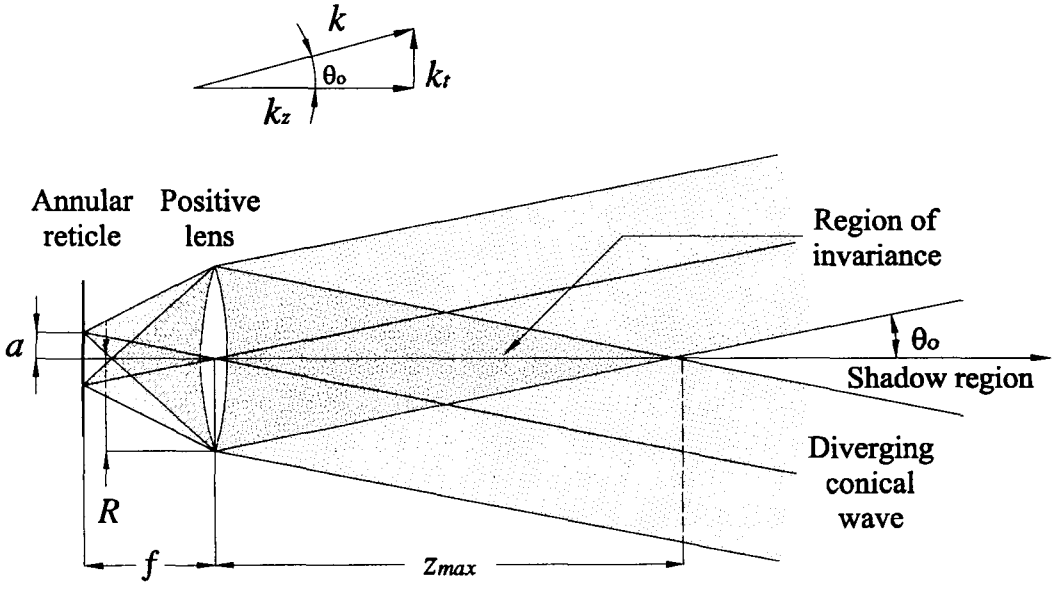

Figure 2.5. Durnin's experimental setup.

Polarization considerations are not made in the analysis so far. However, important asymmetries are introduced in both the near and far field distributions when linearly polarized plane waves are used to generate Bessel beams by means of these the two procedures. Moreover, as the central spot of a Bessel beam is reduced in size, scalar diffraction theory no longer explains in a satisfactory fashion the propagation of sub-wavelength features in the beam. A full vectorial approach is then required [30]. An extensive treatment extending to the nonparaxial region and in full consideration of the effects of polarization states can be readily found in the literature [31, 32].

Bessel beams of arbitrary order and, in general any PIOF, can also be attained by means of holographic techniques. With the advent of fast computational devices, the simulation of the interference pattern of the desired field with a plane wave is transferred to holographic or photographic film. Hence, the resulting hologram is used to reconstruct the field with the aid of a converging lens. The resulting pattern in the film can be regarded as an phase interferogram rather than a hologram in the strictest sense of the term. The interferogram can also be produced by properly modulating a transmission liquid crystal display (LCD). Fig. 2.6 shows the computer-generated holograms for Bessel beams of order $m = 0$ and $m = 5$.

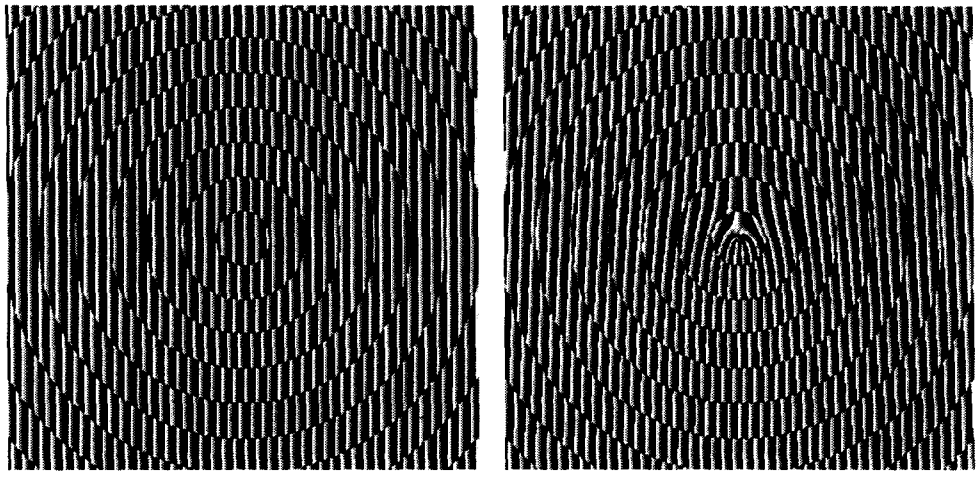

a. Bessel hologram $m = 0$. **b.** Bessel hologram $m = 5$.

Figure 2.6a-b. Computer-generated holograms of two different Bessel beams, fundamental and 5th order respectively. The interferograms were generated with Matlab code as tagged image files (TIFF) in negative gray scale.

Alternate methods for the generation of Bessel beams have been proposed. Specifically, the use of spherically aberrating optics produces an annular pattern whose (dark) center can be additionally blocked with the aid of a circular stop. The size of the stop must be carefully selected in order to avoid diffraction from its edges to significantly affect the field near the optical axis. Resulting zeroth order Bessel beams are outstanding [8]. The use of a Fabry-Perot interferometer and other forms of resonators with specific geometric characteristics have also been proposed for generating Bessel PIOFs [33].

2.2.2 Applications of Bessel beams

Several applications for Bessel beams have been proposed and a number of experiments have been carried out to demonstrate their feasibility. Namely, Bessel beams have been suggested to be used as a tool for optical manipulation in controlled linear guidance and rotation of submillimeter translucid particles. This application makes use of the power distribution of the beams together with radiation pressure in order to control the position or displacement of small macroscopic particles. In one instance, a PIOF was used as a light guide to accelerate and displace Cs atoms [9]. More recently, Arlt *et al.* have used a Nd:YAG laser and an axicon to generate a Bessel-like PIOF in order to assemble polar arrays of silica spheres with a diameter of 2 μm. The same method was used to align a large silica rod in a direction parallel to the propagation of the beam [12]. Given the self-reconstruction attribute of Bessel PIOFs, several colinear samples could be manipulated simultaneously in over spatially separated test cells. In the same manner, it has been proposed that multiple optical interconnects be made using the central region of a Bessel PIOF.

In a more complex application, multiple Bessel beams have been spatially interfered so as to create a volumetric dark region in space that is surrounded by an increasing radiation potential. It has been suggested that such region could be used in single-beam atom trapping experiments [34].

Chapter 3

Rotating Wavefields

Numerous works have directed their attention to PIOFs motivated by their potential applications. As this new class of fields was gradually studied in detail, PIOFs were further classified as self-imaging (SI)and rotating wavefields (RWs). In the most strict sense, neither of these are propagation-invariant; the former posses an intensity pattern that is reproduced after a finite propagation distance and the latter maintain their power distribution upon propagation, except for a rotation in the azimuthal coordinate [35]. In terms of their frequency distributions, both kinds of field satisfy the condition for propagation invariance as their angular spectrum is described by a set of rings - as opposed to one ring - over the sphere of McCutchen.

This chapter describes the general propagation characteristics of rotating wavefields. Special attention is brought to the interference of RWs with plane and spherical wavefronts for reasons that will become evident in this section. Finally, a brief review of the potential applications and current experimental developments regarding RWs is outlined.

3.1 Rotating scalar fields

It was seen in the previous section that the angular spectrum of a complex wavefield $E(\mathbf{r})$ is given by

$$E(x,y,z,t) = e^{i(k_z z - \omega t)} \int_0^{2\pi} A(\varphi) \exp\left[ik_t \left(x\cos\varphi + y\sin\varphi\right)\right] d\varphi. \tag{3.1}$$

The theory outlined in the previous section is also valid for fields not restricted to a constant value of radial frequency. For an arbitrary monochromatic field, however, the radial frequency k_t is not a constant, and thus integration must also be performed with respect to it[36]. For convenience, if both $\mathbf{r}$ and $\mathbf{k}$ are expressed in cylindrical coordinates: $\mathbf{r} = (\rho, \varphi, z)$ and $\mathbf{k} = (k_\rho, k_\varphi, k_z)$, then the spectrum is given instead by

$$E(\rho,\varphi,z,t) = e^{i(k_z z - \omega t)} \int_0^{\infty}\int_0^{2\pi} k_\rho A(k_\rho, k_\varphi) \exp\left[ik_\rho \cos\left(\varphi - k_\varphi\right)\right] dk_\rho dk_\varphi. \tag{3.2}$$

The restriction imposed by the condition in Eq. (2.4)for a field that propagates without change in its power distribution, (apart from a linear rotation upon propagation) can also be expressed as

$$|E(\rho,\varphi,0,t)|^2 = |\exp\left[i\eta(\rho,\varphi,\Delta z)\right] E(\rho,\varphi+\epsilon\Delta z, z+\Delta z, t)|^2, \tag{3.3}$$

with ϵ a constant parameter that defines the direction and the spatial periodicity of rotation of the field, and η is an arbitrary real function. Combining equations (3.2) and (3.3) yields [36]

$$\sum_{m=-\infty}^{\infty} \int_0^{\infty} a_m(k_\rho) J_m(k_\rho\rho) \exp(im\varphi) \left\{\exp\left[i\eta(\rho,\varphi,\Delta z)\right] - \exp[i(m\epsilon + k_z)\Delta z]\right\} dk_\rho = 0, \tag{3.4}$$

where

$$a_m(k_\rho) = i^m \int_0^{2\pi} A(k_\rho, k_\varphi) \exp(-imk_\varphi) dk_\varphi, \tag{3.5}$$

by making use of the expansion

$$\sum_{m=-\infty}^{\infty} i^m J_m(x) \exp(im\varphi) = \exp(ix\cos\varphi). \tag{3.6}$$

Because Eq. (3.4) must hold for all ρ and φ, then the integrand must vanish, and thus:

$$\eta(\rho,\varphi,\Delta z) = \eta(\Delta z) = (m\epsilon + k_z)\,\Delta z + 2\pi n, \tag{3.7}$$

with n an integer. If we require that the phase change $\eta(\Delta z)$ be continuous and set $\eta(0) = 0$, then $n = 0$ and k_z may assume only discrete values $\{k_{zm}\}$ depending on the parameter m. Taking only M terms in Eq. (3.6), the field expression is now

$$\sum_{m=1}^{M} a_m J_m(k_\rho\rho) \exp\left[i(m\varphi + k_{zm})\right]. \tag{3.8}$$

The values of m are defined by $0 \leq k_{zm} \leq k$. From Eq. (3.7) it can be seen that the geometric locus of the angular spectrum is now a discrete set of M Montgomery rings with radii [36, 37]

$$k_{\rho m} = \left(k^2 - k_{zm}^2\right)^{1/2}.$$

Note that for $k_{zm} = k$, the spectrum collapses to a pole on McCutchen's ring, which is the case of a plane wave. On the contrary, for $\beta_m = 0$, the field does not propagate in the z direction. If the values of k_z are not restricted to a discrete set, the result is a nonperiodic rotating beam, as explained below.

The condition for smooth rotation of the transverse intensity in Eq. (3.3) also defines the distance z at which a full rotation of the field is observed, namely:

$$z_R = 2\pi m/k_z. \tag{3.9}$$

In view of this result, a PIOF with no azimuthal structure ($m = 0$) can be thought of as a special case of a rotating wavefield for which $\epsilon = 0$, hence the single-ringed annular spectrum of section 2.1.2.

Although a scalar formalism has been used to derive Eq. (3.7), an extension to vectorial rotating fields has been recently developed by Pääkkönen et al. [30] with the advantage of being suitable for nonparaxial beams. Additionally, an alternate treatment of generalized PIOFs describes an interesting subclass of fields characterized by the aperiodic rotation of the intensity pattern, in the sense that they never return to the original (reference) orientation along the propagation, see for instance refs. [25] and [38].

3.2 Rotating Bessel beams

In the spectrum of Eq. (3.1), it is clear that the parameter m corresponds to an azimuthal phase variation of the higher-order Bessel beam (HOBB).

$$E(x, y, z, t) = J_m(k_t\rho)e^{im\varphi}e^{i(k_z z - \omega t)}. \tag{3.10}$$

In this particular case of PIOF, the spectrum still lies on a single ring but its amplitude is modulated by the continuous complex circular functions of order m. Consequently, HOBBs ($m \geq 1$) show a more complex phase distribution than that of their fundamental counterpart, where only a relative phase change of π is observed between adjacent annuli. These phase changes are related to the zero-crossings of all Bessel functions, as seen in Fig. 3.1. The fundamental Bessel function of the first kind as well as the first three higher orders are shown. Notice that for higher orders there is a minima in amplitude at $\rho = 0$, which is consistent with an indetermination of the phase at this point. For this reason, it is often said that HOBBs have a *phase dislocation* in their center. Note also that the spatial extent of the central minima increases with the order m, which is also evident from Fig. 2.3.

The phase of a HOBB is thus seen to vary in its full range continuously, for a total of m periods in one azimuthal revolution. The phase distribution is best visualized with the aid of Fig. 3.2b for $E(\rho, \varphi) = J_5(\rho)\exp(i5\varphi)$. Note the discrete radial phase variations as opposed to the continuous azimuthal phase gradient. The seemingly discontinuous jumps in the angular direction are due to the phase being plotted only in the $(0, 2\pi)$ range.

Due to the characteristic phase distribution of Bessel beams, the field is strictly rotating as it propagates when the complex distribution is considered. Since the intensity pattern remains unchanged by the local phase distribution, there is no visible effect of rotation in a HOBB propagating by itself.

So far, only Bessel beams have been considered in this section, but it is worth noting that given an arbitrary function $A(\varphi)$ for the angular spectrum in Eq. (2.5), the field can be regarded as a superposition of Bessel fields, or any other set of orthogonal functions.

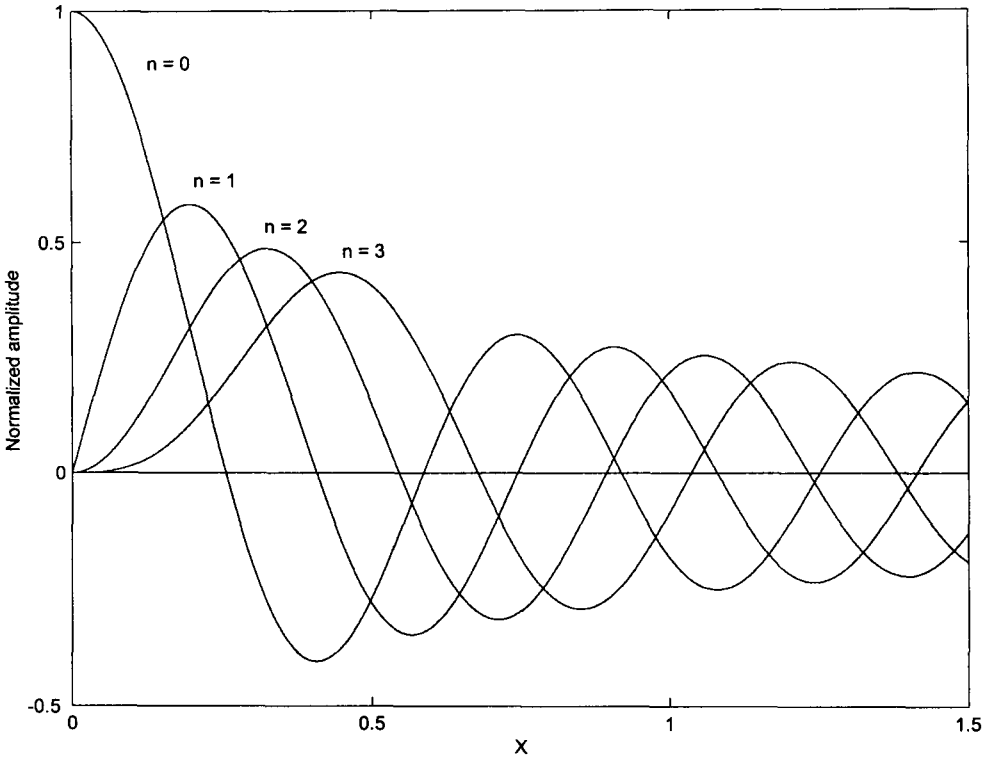

Figure 3.1. Bessel functions of the first kind of order n.

In principle, as along as the phase distribution varies smoothly with the azimuthal coordinate, an arbitrary rotating field distribution propagating with invariant features can be tailored provided the appropriate weights for each component in the set of functions that describes its spectrum are properly calculated and reproduced.

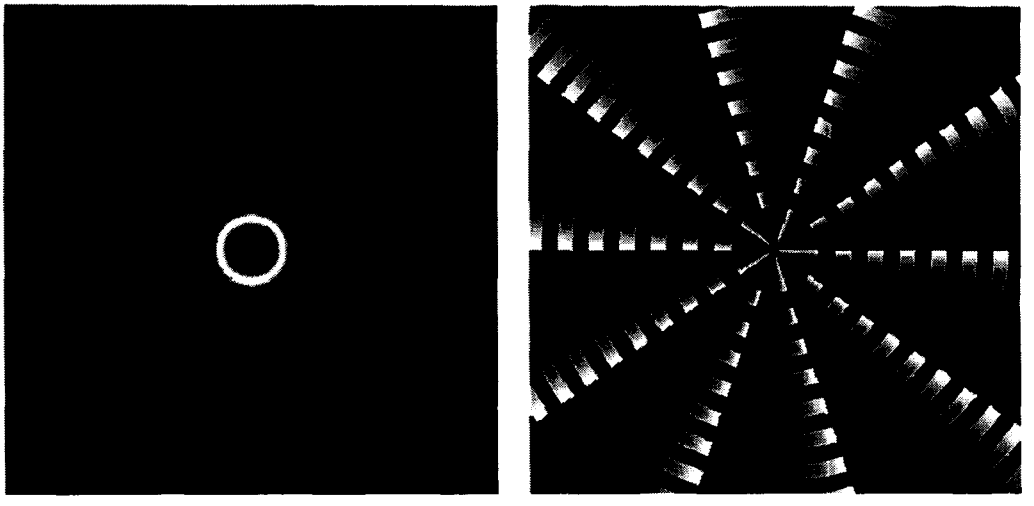

a. $|E(\rho,\varphi)| = J_5^2(\rho)$ **b.** $\arg E(\rho,\varphi) = 5\varphi$

Figures 3.2a-b. Amplitude and phase distribution of a fifth order HOBB. Note the discrete phase jumps in the radial coordinate.

3.3 Interference of higher order Bessel beams

In order to observe and measure the effect of the azimuthal phase distribution in a HOBB, the rotating-phase field can be interfered with a reference plane wave. Since the reference wavefront phase is constant, the differences in phase as the HOBB is interfered with the plane wave can be visualized easily as interference patterns.

One remarkable characteristic of rotating wavefields is that the energy flux can be locally reversed with respect to the direction of rotation or propagation in either the azimuthal or longitudinal direction respectively [15]. The conditions for this are solely given by the parameters of the rotating beam and the plane wave used as a reference.

A second case is that of a HOBB interfering with a spherical wavefront. In this case, the reference wave has a phase distribution that varies radially in a circularly symmetric fashion. This type of interference generates rotating wavefields with interesting spiral patterns, as it will be shown further ahead in this chapter.

3.3.1 HOBBs and plane waves

Consider first the case of a plane wave as reference. The field distribution in this case at an arbitrary value of z and $t = 0$ is:

$$E(\mathbf{r}, \mathbf{t} = \mathbf{0}) = J_m(k_t\rho)e^{im\varphi}e^{i(k_z z)} + E_0 e^{i(kz)}, \tag{3.11}$$

and thus, the field intensity is given by:

$$I(\mathbf{r}) = J_m^2(k_t\rho) + E_0^2 + 2E_0 J_m(k_t\rho)\cos\gamma, \tag{3.12}$$

with $\gamma = m\varphi - (k - k_z)\, z$. From this last term, it is evident that the field undergoes one full rotation after a propagation distance:

$$z_R = \frac{2\pi m}{k - k_z}. \tag{3.13}$$

This distribution is best described as a straight helix with longitudinal period z_R. For an arbitrary time t, a fixed point $P_0 = (\rho_0, \varphi_0)$ is seen to rotate moving forward and "follow" the helical trajectory at an angular velocity ω. Note that since the interference pattern has azimuthal symmetry under a spatial rotation of $2\pi/m$, then m intermediate images of the field are observed at distances:

$$z_{Ri} = \frac{2\pi}{k - k_z}. \tag{3.14}$$

Fig. 3.3 shows the spatial evolution of a Bessel beam of order $m = 3$ made to interfere with a plane wave for one third of a full revolution in steps of $\pi/9$. Note that it is not possible to determine the relative angular rotation of the field were it not for the *a priori* information on the longitudinal period of rotation z_R. A numerical calculation

is useful to determine the order of magnitude of z_R. For a He-Ne laser ($\lambda = 632.8$ nm), and a cone angle $\theta_0 = 1°$:

$$z_{Ri} = \frac{\lambda}{1 - \cos\theta_0} = 4.15 \text{ mm, and} \qquad z_R = m z_{Ri} = 12.44 \text{ mm.} \tag{3.15}$$

The field undergoes one full rotation every 4 millimeters. Thus, for a fixed wavelength, the cone angle alone determines the period of rotation in the frame of reference of the field. It was seen in the previous section that this angle is dependent on the experimental setup used to generate the Bessel beam.

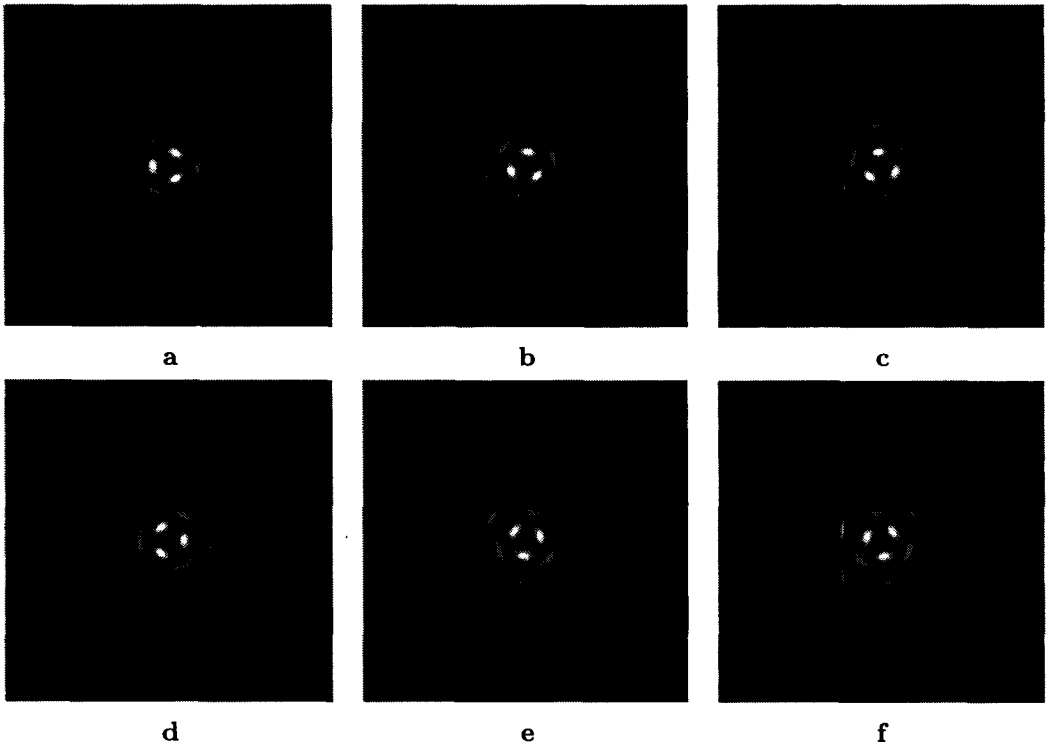

Figures 3.3a-f. Evolution of the transverse intensity distribution of the rotating wave produced by interference of a third order Bessel beam and a plane wave. Total displacement along the propagation axis is 12.5 mm.

The amplitude of the interfering plane wave must attain an intermediate value between the maximum of the Bessel function and the RMS value of the first few lobes. Large plane wave field values will result in poor contrast of the radial modulation.

3.3.2 HOBBs and spherical waves

Spherical wavefronts differ from plane waves in that their phase and amplitude field are functions of the propagation distance and the radial distance from the optical axis. In this case, the interference with a rotating wavefield no longer generates a

perfect image of the field, but the rotation is still easy to visualize near the center of the resulting beam. The radial phase variation of the spherical wave results in a spiral pattern as the phase difference between the HOBB and reference wavefronts is a function of the transverse radial coordinate.

This effect can be visualized in Figs. 3.4a-f. The rotating field corresponds to a Bessel beam of the fifth order. Note that the intensity pattern is imaged very closely over one fifth of a revolution. In this case:

$$E(\mathbf{r},\, t=0) = J_m(k_t\rho)e^{im\varphi}e^{i(k_z z)} + \frac{E_0}{\rho}e^{i(kz)},\ m=5 \tag{3.16}$$

so that the intensity is given by:

$$I(\mathbf{r}) = J_m^2(k_t\rho) + \frac{E_0^2}{\rho^2} + 2\frac{E_0}{\rho}J_m(k_t\rho)\cos\gamma, \tag{3.17}$$

where: $\gamma = m\varphi - (k - k_z)\, z$, as before. Thus the spatial period of rotation is not affected by the curvature radius of the interfering spherical wave.

When a converging spherical wave, the negative magnification of the intensity pattern becomes apparent after a short propagation distance and it appears to "curl" the spiral pattern. If instead, a diverging spherical wave is used for interference, the pattern magnification is positive, resulting in a uncurling effect of the rotating beam and an inversion in the direction of rotation.

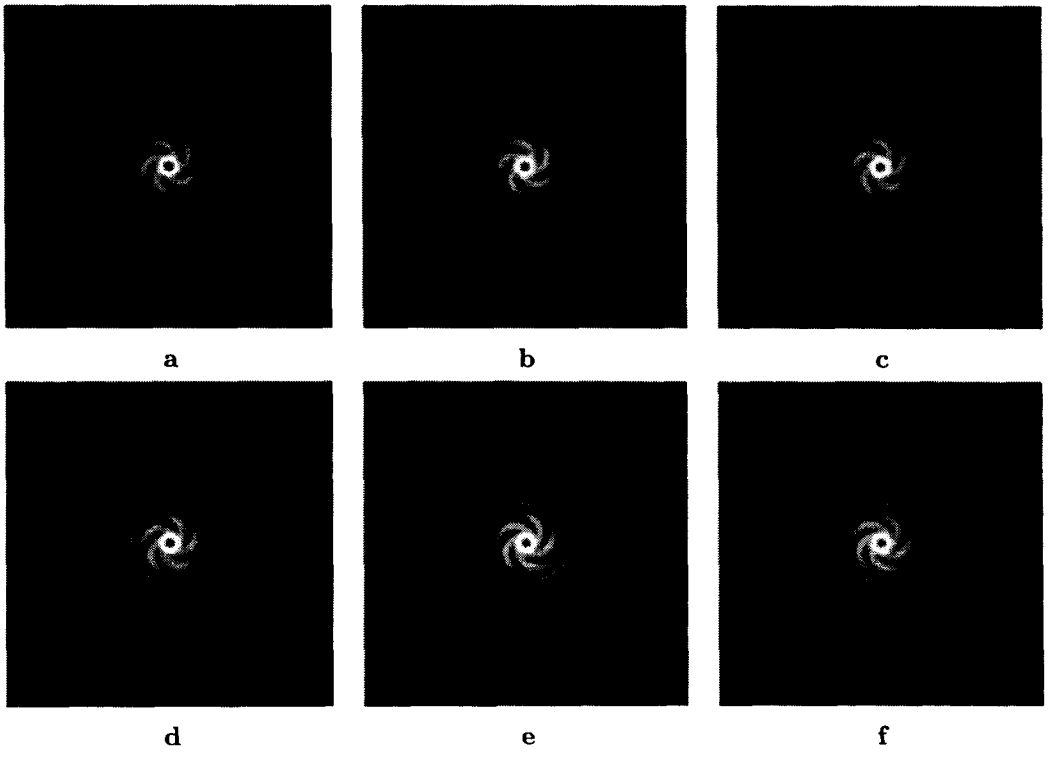

Figures 3.4a-f. Evolution of the transverse intensity distribution of the rotating wave produced with a Bessel beam of fifth order and a spherical wave. Total displacement along the propagation axis is 12.5 mm.

The use of both plane and spherical wavefronts as references in interference with any kind of beam yields a great insight of the phase distribution of the field of interest along propagation. It is this experimental technique that facilitates the close study of complex phase distributions.

3.4 Generation of rotating wavefields

The characteristic phase distribution of HOBBs suggests itself several approaches for their practical generation. Note first that since the phase distribution typically varies harmonically with the azimuthal coordinate, a system with cylindrical symmetry seems indicated only to introduce radial phase changes. Hence, it now seems rather natural to use a conical element to induce the radial distribution on a plane wave.

Experiments involving conical optics are straightforward for the fundamental Bessel beam and it is indeed a very efficient way of attaining the desired beam. However, HOBBs and, in general, other rotating wavefields require a complex field distribution that lead to continuous phase variations in the field. It is this dependence of the azimuthal coordinate that challenges any serious attempt to obtain a rotating wavefield. The problem has been addressed in several different ways, based mainly in the use of either diffractive or refractive optical elements. The first one refers in essence to the use of computer-generated holograms, either phase or amplitude-coded. The advancement of electron-beam lithographic techniques allows for the custom fabrication of wavelength-scale features into transmissive substrates that generate an arbitrary phase distribution [37]. Binary phase diffractive waveplates are also used when electron beam lithography and ion etching techniques are combined [39]. Traditional photographic techniques are also extensively used to generate lower quality holograms on silver halide films. The difference in the quality of the results obtained with either method is proportional to the density of analog storage media, which also determines the optical efficiency of the diffractive device. Additionally, spatial light modulators are often used for the generation of rotating wavefields, with the well-known disadvantage of its discrete spatial grid resulting from pixel coding.

As an alternative, refractive elements attempt to create the local phase delay by means of variations in the optical path of the incident beam. In principle, a material with a constant index of refraction can be carefully shaped to attain the topographic profile associated to the local phase delay that will result in the desired phase wavefront [40]. The amplitude is further modulated by means of linear attenuation. In a recent experiment, the characteristic angular momenta associated to Laguerre-Gauss beams is taken advantage of as the beam is converted into a thin annular wavefield by means of a linear axicon [41]. Since the radial delay is azimuthally symmetric, the phase distribution is preserved in this transformation.

It should be evident by now that the feature that makes rotating beams attractive is also the major technical difficulty in its practical realization. In the present work, a well-known experimental technique is used in a novel way to generate HOBBs. The details of this technique are described in a subsequent section.

Thus far, attention has been focused on RWs that undergo rotation about the optical axis as they propagate. This effect is due to the circular symmetry of the fields associated to Bessel and other kinds of beams. This situation does not fully describe all the possible configurations of rotating beams. In particular, Mathieu (fundamental and odd and even-angular) beams are known to have a field distribution that results in rotation about their interfocal axis along propagation [15].

3.5 Current experimentation with rotating wavefields

Increasing interest has motivated extensive research on the uses and applications for rotating wavefields. Perhaps the most exciting possibility is that of interaction of the radiation field of RWs with matter in the atomic scale. As RWs posses angular momenta related to their rotating intensity patterns, the use of HOBBs or rotating Laguerre-Gauss beams has been suggested as multiple atom traps or *optical bottles* in making use of optical dipole forces [13]. When an atom is radiated with laser light that is blue-detuned with respect to a particular atomic resonance, the dipole force field restricts the atom (or set of atoms) to a region of low-light intensity. In using this principle, multiple regions of field minima surrounded by high intensity field barriers have been proposed as atomic traps [14].

Rotating wavefields could also be used as optical carriers of information, however, any kind of modulation attempted to be made with the rotation characteristics requires first the development of a reliable method for the generation and dynamic shaping of the angular spectrum of the fields.

Chapter 4

Experimental Procedures

Once the theoretical basis for the generation of HOBBs are extensively described in the literature, one may be tempted to take for granted their experimental realization and objective comparison of results with the theory. However, no theory can be complete without verification of its predictions. This chapter describes a simple laboratory setup to produce HOBBs along with several - successful and unsuccessful - attempts to construct the custom optics required for this endeavour. The results of the successful efforts are presented and compared with the respective theoretical predictions.

4.1 Experimental setup

In sections 2.2.1 and 3.4.1, a number of experimental approaches for the generation of RWs in general and HOBBs in particular were discussed. Essentially, generation methods are based in either the use of conical optics combined with phase plates or wavefront reconstruction techniques by means of computer-generated holography. The refractive axicon is sometimes replaced by the ubiquitous circular slit. It has been seen that the major difficulty in generating a HOBB rests in the continuous phase distribution of their angular spectrum.

The subject of the present work is the experimental verification of a simple and original method for the generation of HOBBs. The technique was proposed by Gutiérrez-Vega [15] and is founded in the physical understanding of the nature of RWs. As a result of the mathematical principles outlined above, the approach is novel in principle and its implementation suggests a natural setup. In order to derive the operating principle of this method, let us review the plane wave decomposition of a HOBB:

$$J_m(k_t\rho)e^{im\varphi} = \int_0^{2\pi} e^{im\varphi} \exp\left[ik_t\left(x\cos\varphi + y\sin\varphi\right)\right] d\varphi. \tag{4.1}$$

Where: $\rho^2 = x^2 + y^2$. Using:

$$\mathcal{F}\{\delta(r - r_0)\} = 2\pi r_0 J_0(2\pi r_0 \rho) \tag{4.2a}$$

$$\frac{1}{k_t}\mathcal{F}\{\delta(r - r_0)\} = J_0(k_t\rho) \tag{4.2b}$$

with $\frac{r_0}{2\pi} = \frac{1}{\lambda}\sin\theta$ the spatial period in Fourier space, then Eq. (4.1) can be rewritten in a more compact form in terms of the Fourier transform, as:

$$\mathcal{F}\{\delta(r - r_0)e^{im\varphi}\} = k_t J_m(k_t\rho)e^{im\varphi}. \tag{4.3}$$

The right-hand side of Eq. (4.3) represents a field that is proportional to the m-th Bessel function of the first kind. This expression is also interpreted as the operation of a system that performs the Fourier transform of the input field $E_i = \delta(r - r_0)e^{im\varphi}$ and results in the Bessel field. It is this delta function that directly suggests the generation of a fundamental Bessel beam using Durnin's experiment with an annular slit for $m = 0$. By using Euler's identity, the complex part of the left hand side of Eq. (4.3) can be further decomposed so that:

$$\mathcal{F}\{\delta(r - r_0)(\cos m\theta + i\sin m\theta)\} = k_t J_m(k_t\rho)e^{im\varphi}, \tag{4.4}$$

$$\mathcal{F}\{\delta(r - r_0)(\cos m\theta) + i\delta(r - r_0)\sin m\theta\} = k_t J_m(k_t\rho)e^{im\varphi}. \tag{4.5}$$

Thus, in order to obtain the Bessel field distribution on the RHS of Eq. (4.5), the complex transmittance in brackets would have to be fed into a Fourier transform system. The functional form of the transmittance slit suggests the geometrical means to achieve this. Since there are two annuli with different angular modulations, one purely real and one purely complex, an arrangement of two field sources with the appropriate angular modulation can be proposed. For instance, an amplitude-splitting interferometer such as the Mach-Zehnder. The Bessel distribution is being attained by means of adding together the odd and even angular parts of the desired Bessel field. A plane wave incident in transmissive optical elements with the transmittance functions:

$$t_1(\theta) = \delta(r - r_0)\cos m\theta \tag{4.6a}$$

$$t_2(\theta) = i\delta(r - r_0)\sin m\theta \tag{4.6b}$$

would serve this purpose. The binary annular transmittance represented by the Delta function is to be modulated in both amplitude and phase. Note that the relative phase of both t_1 and t_2 is constant and that the transmission functions attain both positive and negative values in the full range of θ. The factor i in t_2 represents a phase shift in t_2 relative to $t_1$in the value of the field independent of θ, that is, a temporal phase shift equivalent to a relative phase delay. In terms of optical elements, two identical binary annular slits with modified transmittance over the angular coordinate can be used to generate initial fields:

$$E_{01}(\theta) = E_0\delta(r - r_0)\cos m\theta, \tag{4.7a}$$

$$E_{02}(\theta) = iE_0\delta(r - r_0)\sin m\theta. \tag{4.7a}$$

A quarter-wave retarder can be introduced in the optical path of E_{02} in order to induce the relative temporal delay with respect to E_{01}. Once obtained, carefully interfering the fields and performing the Fourier transform with a well-corrected lens will result, in principle, in:

$$\mathcal{F}\{E_0\delta(r - r_0)(\cos m\theta) + i\delta(r - r_0)\sin m\theta\} = \tag{4.8a}$$

$$E_0 k_t J_m(k_t\rho)\{\cos(m\varphi) + i\sin(m\varphi)\} = E_0 k_t J_m(k_t\rho)e^{im\varphi}. \tag{4.8b}$$

The modulus of the circular functions can be achieved by means of properly overexposed photographic film. Regarding the phase transfer function, since there are $m+1$ sign changes in the phase of t_1 and t_2 in one full range of θ, then in principle, a set of $1/2$ wave retarders can be introduced in the appropriate positions of the film so to act as phase inverters and provide for the required phase distribution. The suggested optical setup is shown in detail in Fig. 4.1. Note that, since: $\sin\theta = \cos(\theta - \pi/2)$, then except for a rotation in their relative angular positions, t_1 and t_2 are physically identical. Care must be taken in order to ensure that the optical axes of the retarders are properly aligned with respect to both the incoming field and the fast axis of the $1/4$-wave retarder. Note also that at the converging lens L_2, located exactly one focal length from either slit operates the Fourier transform on the resulting field. Simple as it may seem, the setup thus requires precise alignment of the different component beams in order to obtain the desired result upon interference.

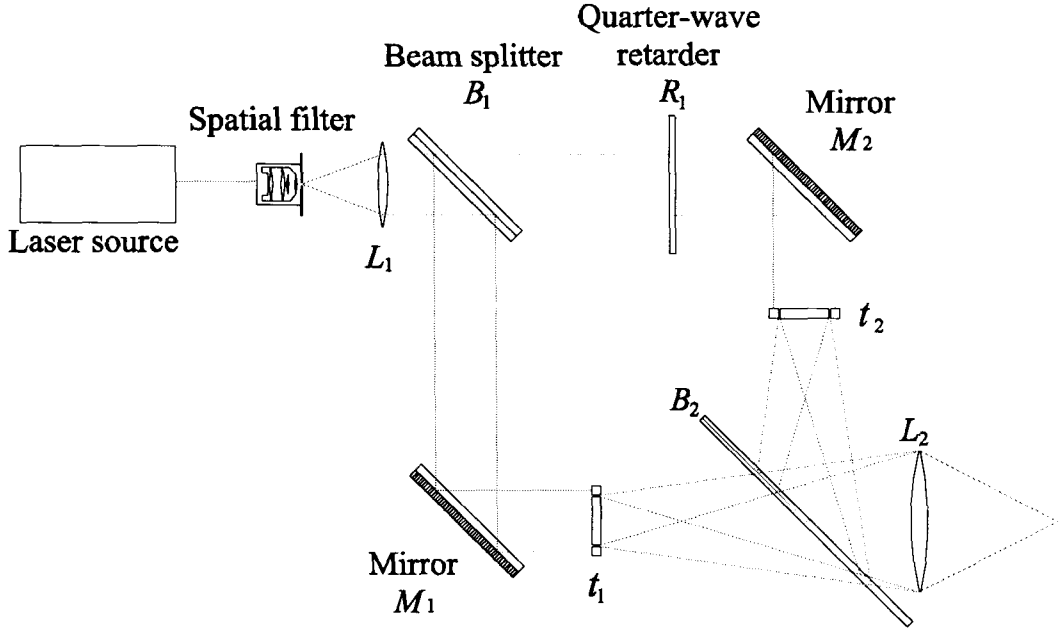

Figure 4.1. Suggested experimental setup to generate HOBBs.

In view of Eq. (??), it is evident that E_{01} and E_{02} evolve into the orthogonal components of the Bessel beam. Hence, it is strictly adequate to say that the setup generates the Bessel wavefield by first producing its odd and even components and then adding them together at the output of the interferometer. It is important to point out that in practice, the transmittance functions t_1 and t_2 can only be close approximations of the ideal delta functions, for any real annuli must have finite widths and these are not necessarily uniform up to wavelength scale. Formally, the Fourier transform of a real circular slit, $t_R(r) = 1$, $r_0 < r < r_1$ is given by [29]

$$\mathcal{F}\{t_R(r)\} = \frac{r_1 J_1(2\pi r_1 \rho) - r_0 J_1(2\pi r_0 \rho)}{\rho}, \tag{4.9}$$

so that:

$$\lim_{(r_1-r_2)\to 0} \mathcal{F}\{t_R(r)\} = 2\pi r_1 J_0(2\pi r_0 \rho), \tag{4.10}$$

by use of L'Hospital rule. Clearly, the result will get increasingly close to the expected interference pattern when the annuli are built as thin as possible within reasonable limits.

4.2 Description of experimental techniques

From the above discussion, it should be evident by now that the key elements in the Mach-Zehnder interferometer are the complex plates described by $t_1(\theta)$ and $t_2(\theta)$. The approach to construct these components was to split their complex transfer functions in their real and imaginary parts and build them separately. Overlapping the phase changes has an overall practical advantage over attempting to build the complex function. For instance, given:

$$\left.\begin{array}{l} t_1(\theta) = \cos\theta = s_1(\theta)\,|\cos\theta| = s_1(\theta)a_1(\theta) \\ t_2(\theta) = i\sin\theta = is_2(\theta)\,|\sin\theta| = s_2(\theta)a_2(\theta) \end{array}\right. , \; 0 \le \theta < 2\pi, \tag{4.11}$$

with:

$$\left.\begin{array}{l} s_1(\theta) = \left\{ \begin{array}{c} 1,\ 0 \le \theta < \pi/2 \\ -1,\ \pi/2 \le \theta < 3\pi/2 \end{array} \right| \\ s_2(\theta) = \left\{ \begin{array}{c} 1,\ 0 \le \theta < \pi \\ -1,\ \pi \le \theta < 2\pi \end{array} \right| . \end{array}\right. \tag{4.12}$$

For implementation, it is easier to think of each one of $t_1(\theta)$ and $t_2(\theta)$ as the product of an amplitude transfer function and a phase reversal function. The amplitude now varies as the absolute value of the circular functions, whereas the phase is reversed where appropriate according to their sign. Ergo, overlapping a gray scale plate $a_1(\theta)$ and a phase plate with $s_1(\theta)$ will result in an effective amplitude transfer function $t_1(\theta)$. Note that the values of $a_1(\theta)$ are real for all θ, whereas the domain of $s_1(\theta)$ has only two possible values (see Fig. 4.2a-d).

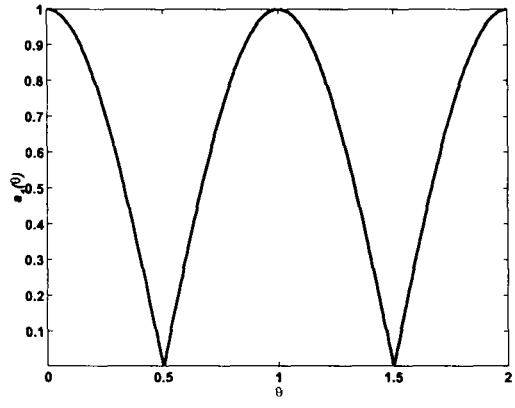

Figure 4.2a. $a_1(\theta) = |\cos(\theta)|$.

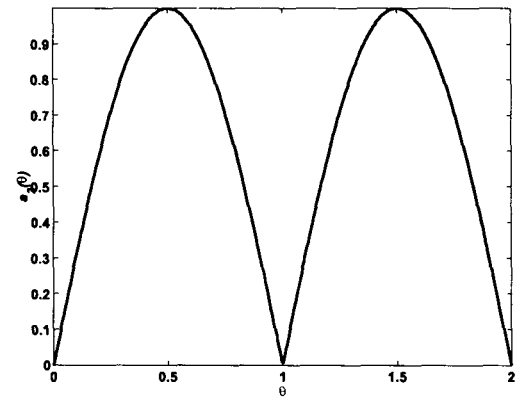

Figure 4.2b. $a_2(\theta) = |\sin(\theta)|$.

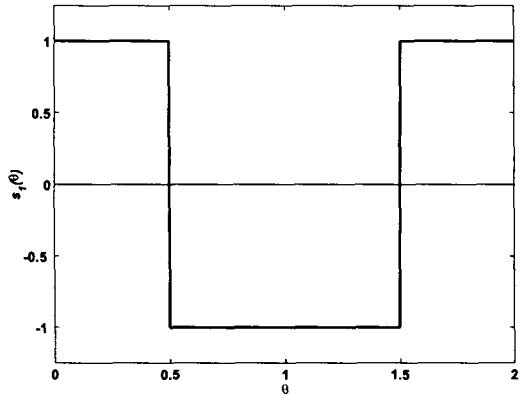

Figure 4.2c. $s_1(\theta)$.

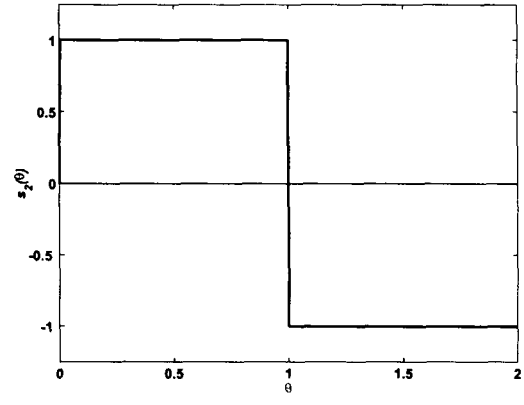

Figure 4.2c. $s_2(\theta)$.

The same holds true for any value of m other than $m = 1$, as discussed here, with the consequential added complexity in the phase plates $s_1(\theta)$ and $s_2(\theta)$, as the number of zero-crossings increases linearly with m. Several attempts were made to obtain reasonably accurate amplitude and phase plates with limited financial resources, some of which are described below.

4.2.1 Photographic techniques

Theoretically, an arbitrary amplitude modulation of monochromatic light can be performed by means of a gray scale plate. Such plate can be constructed by several means, the less expensive of which is, by far, exposition of photographic film with the desired modulation $t_F(q_1, q_2)$ for positive film, or its supplementary normalized counterpart: $1 - t_F(q_1, q_2)$ for negative film. Here (q_1, q_2) stand for the transverse coordinates. Experimentally, complications in the modulation can arise primarily from two sources: first, the dynamic range of the values between the desired transmittance minima and maxima and secondly, the functional variation of the target transfer function. In the first case, if the range is small, the variations must be resolved by pushing the film developing process to attain the largest number of values between minima and maxima,

the limit being set by the sensitivity vs. time curve for a particular film. Adjusting for the logarithmic response is necessary and for a particular amplitude field transfer function the optimal adjustment is obtained by experimentation. In the latter case, very small sections of low transmittance in the vicinity of rapidly varying halftones is best obtained by a configuration of multiple films, so that the zero-transmission regions are attained but some resolution in the vicinity is lost. Here, the adjustment is linear, but it is important to note that unexposed film is far from totally transmissive and thus a uniform obscuration of about 26% is typically observed at 632.8 nm.

In order to obtain the angular transmittance functions $a_1(\theta) = |\cos\theta|$ and $a_2(\theta) = |\sin\theta|$, tests were conducted with Pan-F Plus black and white negative film ISO 50 from ILFORD. The film was bracketed towards overexposure at one-half stop steps from 1/1000 to 5 seconds. The development process was realized with Kodak HC−110 at room temperature using water for stop bath. The film was then fixed with a dilution of Kodak Rapid Fixer in normal concentration as recommended by the manufacturer. Typical resolution for this film with the above process was found to be 90 lines per millimeter (lpm). The complementary amplitude transmittance functions:

$$t_{c1} = 1 - |\cos(\theta)|\,, \tag{4.13a}$$

$$t_{c2} = 1 - |\sin(\theta)|\,, \tag{4.13b}$$

were generated by a 1024×1024 value matrix in matlab and displayed in a liquid crystal display properly set to neutral bright and contrast values. The value range of each matrix element could vary from 0 to 1023 in halftones of gray. The film performed poorly since the zero-exposure transmission proved to be too lossy and considerable obscuration limited the contrast of the amplitude behind the plate. In order to compensate for this, the film was replaced with Kodak Technical Pan black and white negative film ISO 100. Contrary to what one would expect, one can push the developing process up to 190 lpm or better for this film. This fact becomes reasonable as ILFORD film is designed with graphic arts applications in mind. The main advantage of Technical Pan film is, however, its high transmittance at zero exposure. Since the film is not strictly rigid, one must carefully stretch the film uniformly before attempting to mount it in the interferometric setup.

Once the angular amplitude modulation was achieved, there remains the construction of the annular slit. A photographic approach was first attempted using a backlit semi-translucid white paper with a thin circular annulus drawn on it with black organic ink. Even though the slit was imaged on the film at very high resolution, the contrast of the film is not good enough to produce the desired diffractive effect. Multiple films were carefully overlapped to improve contrast, but in this case the absorption was too high for practical detection of the diffractive pattern as the total transmitted power is severely reduced even at only two-film combinations.

On a second attempt, two concentric circular cuts were made on an opaque vinyl self-adhesive film. The cuts were performed by a CNC diamond cutter driven by an MS-Windows compatible driver and given binary input with Corel Draw. Several combinations of diameters were essayed; however, the cutter would consistently tear the

film apart due to the small radii of the circles. The outcome would typically be an offset inner circle and a considerable ripple around the circumferences resulting in highly irregular and large annuli. As this deviation of optical methods proved to be too rough an approach, it was an obvious step to go back to photographic techniques and find a way around the low contrast issue.

4.2.2 Lithographic techniques

Lithography is actually a broad term that encompasses all methods of producing a contact negative of a desired print that is then transferred onto media by either mechanical, chemical or optical methods or a combination of these. In this work, the term lithography refers strictly to photolithography. In essence, photolithography is different from photography only in that the positive final prints are produced by contact negative masks in the former whereas optical magnification (or reduction) of the negative is taken advantage of in the later technique.

There is a fundamental difference in lithographic film when compared to black and white photographic film[1]. Namely, that the range of lithographic film is binary; that is, the film can be totally transparent or totally opaque within the domain of a single grain. As a consequence, it is practically impossible to obtain halftones out of lithographic film due to its high contrast, but this is clearly advantageous for the construction of the slit.

After multiple tests, it was found that a circle of diameter $\phi = 1500 \pm 25$ μm and thickness $\delta \simeq 22 \pm 3$ μm was easily achieved by photoreduction of a positive black circular ring printed on white bond paper. The positive print was done with a black and white laser printer at 150 dots per inch (dpi) with an original ring diameter of 7.5 mm and a 1/4 point (pt) ring thickness - approximately 88.2 μm -. The reduction was done at 20% with an AGFA photoreducer using AGFA orthochromatic line film. Theoretically, the thickness of the ring could be reduced to 17.6 μm, however, the film is difficult to push while developing as the sensitized emulsion is removed in the process, whereas the opposite occurs in photographic film.

The diffraction pattern that results when a plane wave impinges on the ring is shown in Fig. 4.3. Since the wavefront was not further focused, this is not strictly a Bessel PIOF. Note also that the vertical scale is normalized to the expected maximum of the Bessel distribution. The observed truncation at approximately 35% of this value is due to saturation of the (uncompensated) CCD sensor in the camera.

As the lithographic mask served the purpose of generating the intended distribution, an attempt to emulate the angular transmittance function with binary modulation was made. The benefit from this approach would be a single amplitude plate that would serve as the radial delta function and angular amplitude modulator as well.

Evidently, this approach would be successful as long as the binary approximation to the circular functions is close enough not only in density, but also in regards to the

[1] Sensitivity of photolithographic film is dependent of the wavelength that the film is exposed to, in particular orthochromatic film is practically insensitive to red light, as opposed to panchromatic film, with a nearly flat sensitivity across the entire visible spectrum.

local variation or rather, the slope that describes the local changes in halftones.

A photolithographic infrared laser printer was used to generate the discrete amplitude modulation on photolithographic polyester film. Even though the modulation is in average equivalent to the intended circular function, the interference patterns show sensitivity to the discrete dotted distribution used to approximate the continuously varying sinusoidal functions.

Figure 4.4 shows the diffraction patterns that result when using the outcoming masks from this process for several values of m. Note that although the patterns do resemble the general functional form of the theoretical patterns on the left column, there exists a broad apparent discontinuity in the region of minima. Additionally, a considerable ripple can be observed along the annular sections of the patterns that is not explained by the irregularities of the ring, but rather by the border waves that the discrete amplitude modulation produces added to the finite extent of the annular slit. The photographs were obtained with a black and white 1/3 in charge coupled device (CCD) camera. Ripple of the annular lines of 1% random has been accounted for in the simulation.

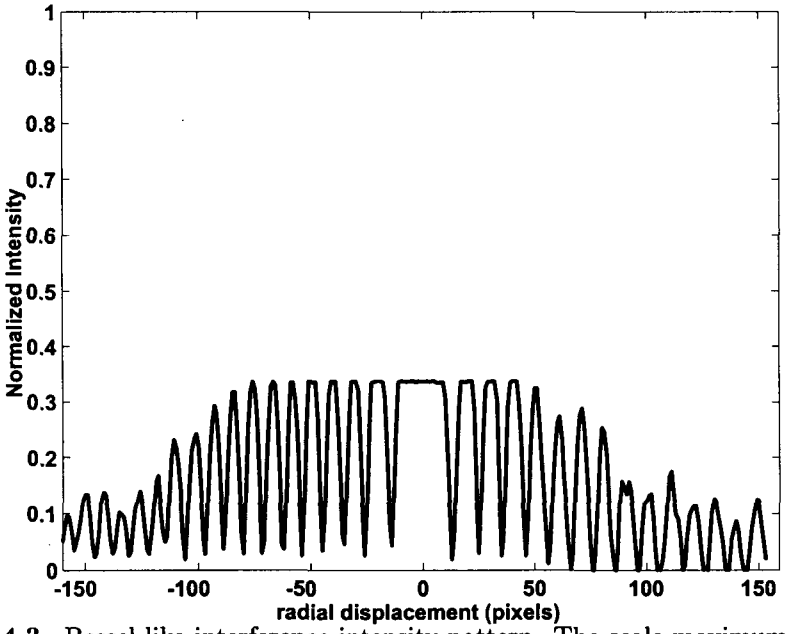

Figure 4.3. Bessel-like interference intensity pattern. The scale maximum is set to the peak value of the theoretical zeroth order Bessel transverse intensity (not shown).

In general, lithographic techniques proved to be appropriate for binary masks but its use in masks with continuous amplitude modulations is far from adequate. Unfortunately, the balance between the high contrast of the annular slit and the gradual distribution of halftones along the angular coordinate was not attained in one single lithographic filter. Thus, separate plates for each purpose were generated and over-

lapped using registration marks and a microscope (see Fig. 4.5).

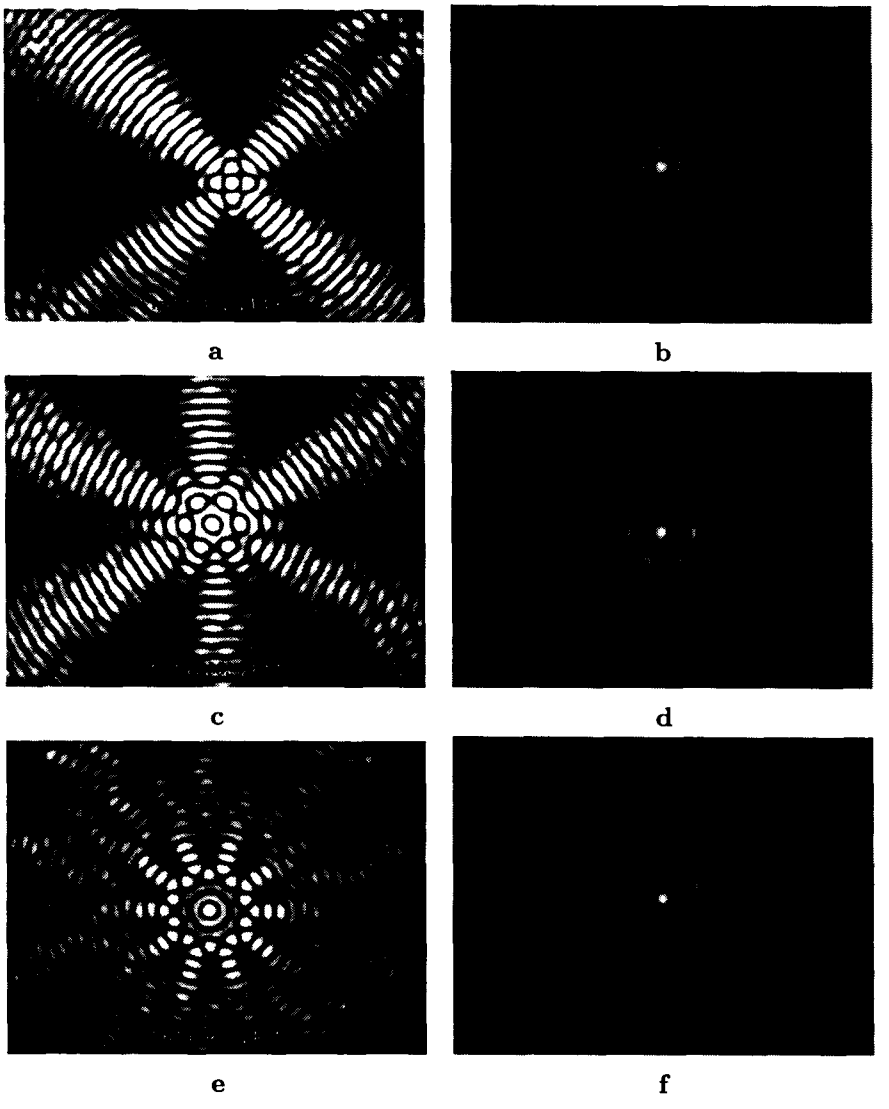

Figure 4.4a-f. Experimental (left column) and theoretical diffraction patterns for absolute-value circular functions. a)-b) $|\sin 2\varphi|$, c)-d) $|\cos 3\varphi|$, e)-f) $|\cos 5\varphi|$.

It is important to note that at this point no phase modulation has been embedded onto the plates. The result from overlapping the multiple films and retarders is shown

in Fig. 4.6.

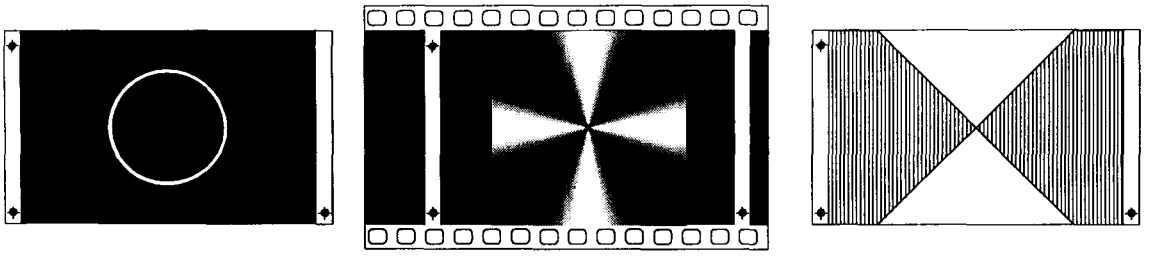

Figure 4.5. Overlapping of multiple plates to obtain the desired transmittance function.

Figure 4.6. Resulting transmission plate (grating detail).

4.2.3 Phase retardation methods

From the above discussion regarding the construction of the complex plates, it may appear that the local phase changes required for the construction of the Bessel beam is as straightforward as the amplitude modulation. In principle, that is the case. The procedure is simple: for a circular function $\cos(m\theta)$, one requires m phase inversions every π/m radians. A half wave retarder can then be placed in the amplitude plate covering this angular extent for every sign reversal of the phase.

In practice, the retarders can be sliced as circular segments off from a mica or quartz half wave phase plate. When using mica, caution must be used to keep the fast axis properly oriented relative to the polarization vector of the laser source. In the case of quartz, or any other birefringent crystalline material, every section must be obtained from the crystal growth direction and all with the same thicknesses, so to avoid unwanted phase shifts in the residual components of the linearly polarized laser source.

Triangular sections were cut from a cellulose acetate butyrate (CAB) supported polyvinyl-alcohol clear film calibrated to one half wave in the 560 to 820 nm range at 0.01 in. thickness. The film was sectioned using a surgical blade and a microscope. Each section was then placed on the negative side of the amplitude plate (ring and negative) and bonded with cellulose tape well away from the optical path of the incident beam. The transmission figure at incident light for the retarder film is 92%, with a phase uniformity of 8% according to the manufacturer. The size of the vicinity where the maximum variation in phase is attained is large compared to the thickness of the ring,

which makes it difficult to notice any inhomogeneity upon transmission. Since the fast axis is sensitive to transverse misalignment, the placing of the retarding sections must be made only after the negative film has been stretched and overlapped to the lithography with the ring. Note that even though both plates have identical transmission complex functions, the relative spatial rotation amongst them forbids from using two equal plates, for such rotation would modify the relative alignment of the polarization vector of the source field and the retarders. A typical (overexposed) focused interference pattern from the prototype plate for $m = 2$ is shown in Fig. 4.7a. Notice that, again, the overall distribution of the intensity does resemble the expected pattern but the angular minima are considerably more extended. In addition, the experimental result is significantly irregular, in particular, a consistent ripple in the ring segments can be observed. This irregularity is attributed to the border waves that arise from diffraction off of the edges of the retarder sections and the finite extent of the annular aperture.

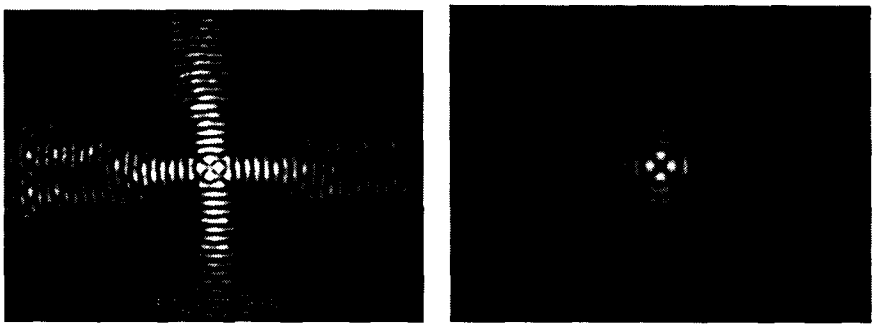

a b

Figures 4.7a-b. Experimental and theoretical diffraction patterns using CAB-polyvynil-alcohol retarders for $m = 2$.

Given the poor performance of film retarders, an alternate approach for the phase transfer function was tried. This time, instead of recurring to a birefringent material in order to rotate the polarization vector locally, a change in optical path was introduced, thus resulting in a phase shift of one half wave[2]. In order to achieve this, a thin (30 μm) silica plate was inserted at the proper locations on the amplitude plate to account for the delay. The optical path difference had to be set to a fixed value so that the phase shift $\Delta\phi$ complies with:

$$\Delta\phi = kn_G d \sin\gamma = \pi(1 + 2l), \quad l = 0, 1, 2, \ldots \tag{4.14}$$

where: $n_G \simeq 1.50$, is the refractive index of the glass plate, d its thickness and γ is the relative angle between the plane of the silica plate and the amplitude plate. The first angle γ at which a half wave phase delay can be achieved is:

$$\gamma = \arcsin\left(\frac{\lambda}{2n_G d}\right) \simeq 0.40°. \tag{4.15}$$

In the actual experiment, the angle γ is slowly varied to attain the lowest value possible so that the reflection loss remains small and lateral deviations of the beam are negligible.

[2]In fact, for a linearly polarized field, a spatial and a temporal phase delay of π are equivalent.

Since glass is a brittle material, the main disadvantage of this method is the difficulty in cutting the glass plates to an arbitrary size. Since silica plates are available in rectangular shape, they are particularly suitable to be used in an experiment with $m = 1$ without the need for cutting or shaping[3]. The intensity distribution at the Fraunhofer plane after a typical plate with glass phase inverters is depicted in Fig. 4.8a. Note that the result is in better agreement with the theoretical expectations (Fig. 4.8b) when compared to previous results using polyvinyl-alcohol phase retarders.

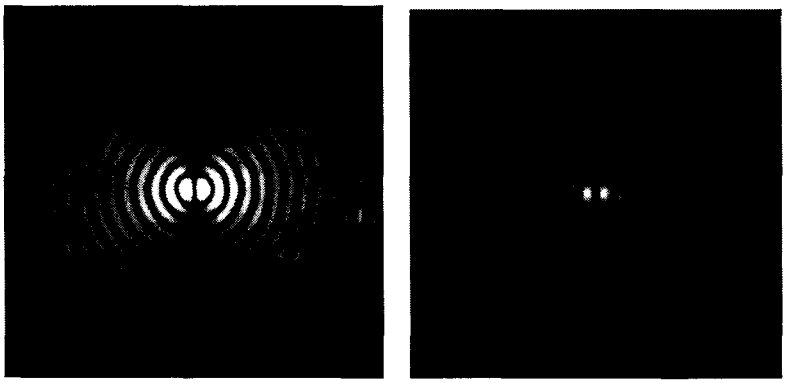

a b

Figures 4.8a-b. Experimental and theoretical diffraction patterns using glass retarders $m = 1$.

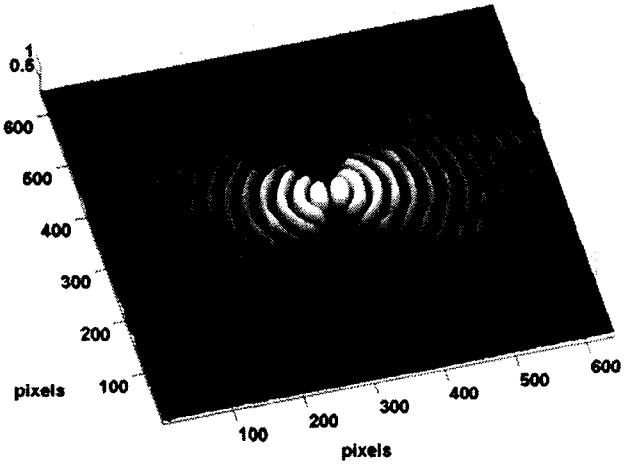

Figure 4.8c. Transverse intensity profile surface plot.

Glass is indeed a more reliable material for the purpose of retardation, as limiting the variations in its thickness is a relatively easy process. The high purity of optical glass is also easily achievable. Because of this, the quarter-wave retarder is also more convenient to implement with glass, as long as the tilt angle is set to the proper value in

[3]Mostly for this reason, the experimental work described in the next section focuses almost entirely on the case $m = 1$.

accordance with Eq. 4.14 for $\pi(1+2l)/2$. One disadvantage of glass over film is, nonetheless, its brittleness, which complicates the integration of the slides in the experimental arrangement.

4.2.4 Assembly procedures

Once the custom optical elements have been described and constructed, some details must be carefully accounted for in order to obtain successful results from the interferometric setup described in the previous section.

Firstly, as the glass slides must lie at a small angle γ with respect to the amplitude plates, each one of them (m for each arm) are now to be attached to rotary mounts where this angle can be varied with high precision, namely, of the order of 0.1°. The amplitude plates are to be set at a an angle of 90° with respect to each other, and for this purpose, at least one of them is also to be placed on a rotary mount orthogonal to the propagation axis. The glass slide that will serve as quarter-wave retarder in one arm of the interferometer is required to be tuned to that precise retardation, again, a rotary mount is prescribed. At this point, there are $2m + 2$ angular variables to be set before interference is observed. Evidently, it is advisable to attempt the experiment first with the lowest value of m.

In order to obtain the desired phase distribution upon interference at the output of the interferometer, the laser source must be linearly polarized. As the glass retarders are to be tilted in the direction of the slow axis, circular (or elliptical) polarization of the source would result in added complexity of the experiment and an interference pattern that is a superposition of two rotating Bessel beams with orthogonal polarization states, resulting in a phase distribution that will depend on the relative magnitude of the field components.

4.2.5 Setup integration

Because the spatial structure of the beams to be interfered presents small features, it is desired to construct the Mach-Zehnder interferometer so that the arms are as short as possible. Also, since an important feature of the experiment is the invariant distance of the resulting HOBB, the separate beams are to be carefully aligned over a long distance within the spatial limits of the laboratory.

For the actual experiment, the light from a 25 mW He-Ne laser (632.8 nm) was first spatially filtered by focusing it with a 10X objective into a 25 μm Al pinhole. The lens L_1 ($f = 2.54$ cm) was used to form the collimated beam that would serve as the input to the interferometric setup. The beam was split and its components reflected in the mirror M_1 and M_2 (surface figure: $\lambda/4$) at right angles. At this point, the quarter-wave retarder was introduced in path 2 of the interferometer. The beams passed through the plates t_1 and t_2 and the resulting diffraction patterns were added at the nonpolarizing beam splitter B_2. The length of the optical path between the beam splitters is set to 12 in. The lens L_2 ($f = 6$ in, $R = 2$ in and: $f = 15$ in., $R = 5$ in used in another instance) focuses the output beam to the invariance region. All components were mounted on an

optical breadboard bench. A photograph of the experiment is shown in Fig. 4.9.

Figure 4.9. Actual experimental setup.

Records of the intensity distribution at different distances from L_2 were obtained by two different methods. First, a single-lens reflex 35 mm photographic camera with the lens removed was used. Best exposure times were found to be within the 1/125 to 1/500 s range. Alternatively, a charge coupled device (CCD) black and white composite video camera connected to a frame grabber was also utilized for this purpose. Because of the limited dynamic range of the CCD sensor and its sensitivity in the near infrared, a neutral density filter was used at the input pupil. Exposure time in this case was set by the automatic bright control and white balance of the frame grabber. The cameras (not shown) were mounted on an optical rail that allowed displacement in the direction of propagation.

4.3 Experimental results

In general, an experiment is intended to demonstrate the predictions and results of theoretical work. Due mainly to the relentless nature of reality, it is often hard to construct the adequate source for a particular effect. Sometimes, the difficulties are found in the observation method for the desired phenomenon. The outcome of an experiment must then be carefully analyzed and its deviations from theory explained in the best possible manner. This section presents and describes the results recorded from the experimental setup described in the two former sections.

4.3.1 Preliminary results

Once the setup has been fine-tuned, the odd and even components are generated and inspected independently to determine its suitability for interference. Clearly, the

components must not only match the theoretical expectations but they must also be identical except for a 90° spatial rotation. Fig. 4.10a and 4.10b are depictions of the Bessel-sine and Bessel-cosine components respectively.

a. Bessel-cosine. **b.** Bessel-sine.

Figures 4-10a-b. Transverse intensity profiles for Bessel odd and even components.

Generation of a rotating Bessel beam requires first the proper generation of a HOBB. The most critical factor in attaining this proved to be the proper phase delay between component beams. A small deviation in this was prejudicial since the phase delay varies largely with small tilt angle variations of the glass plate. Also, the lateral displacement of the beam, although relatively small, is non-negligible when the dimensions of the features of the HOBB are considered. In Fig. 4.11a, the effect of a relative global phase shift of $\Delta\phi = 3\pi/4$ between the components over the interference pattern at the output of the Mach-Zehnder interferometer is shown.

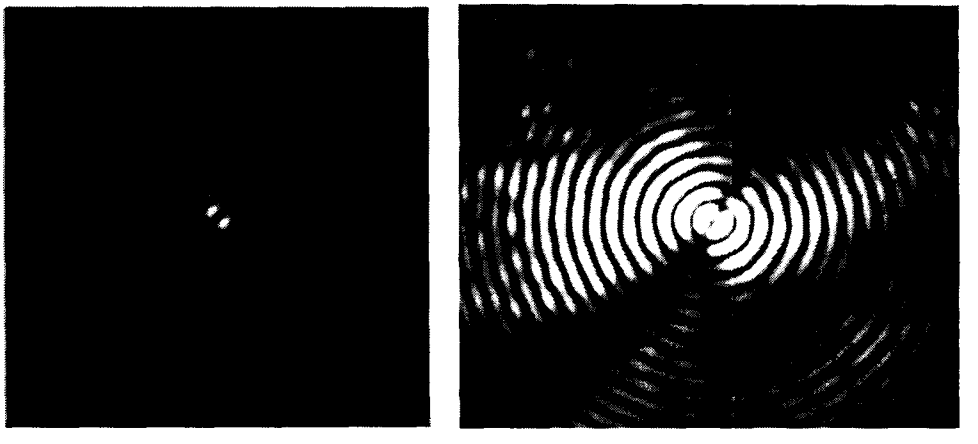

a. Theoretical. **b.** Experimental result.

Figures 4-11a-b. Interference of first order Bessel components witha relative phase shift.

Compare to the actual experiment in Fig. 4.11b, and note that local relative phase shifts are also present, which is evidenced by dark regions. In particular, close to the center on the right lower region where the seventh and eighth annular regions vanish. After repeated experimentation, these phase shifts were found to be caused by local deformation of the lithographic films in the grating.

4.3.2 Results from interference

Proper correction of the aforementioned deformation and careful alignment of the interferometric setup allows for the production of a first order Bessel beam, which can be seen to present good circular symmetry albeit the ubiquitous ripple in the outer lobes (Fig. 4.12).

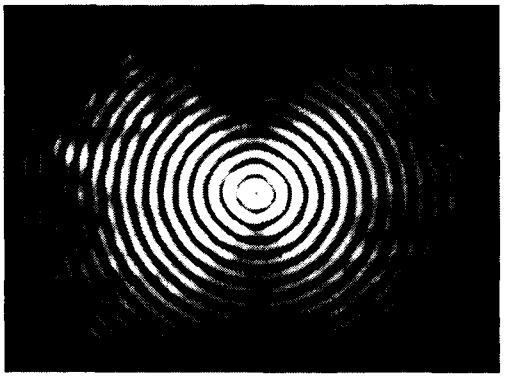

Figures 4.12. First order Bessel beam.

Perhaps the most characteristic feature of HOBBs, and certainly one of the main motivations of the present work is precisely the minimum at their origin. Naturally, one would expect this to be easily observable, but Fig. 4.11 is evidently contradictory in this respect. The poor visibility, or rather, the relatively small dimensions of the minimum are best explained by the large relative amplitude of the first lobe in $J_1^2(k_t\rho)$. The normalized amplitude of this intensity function is shown in Fig. 4.13. This distribution corresponds to the Fourier transform of an infinitely thin circular ring, which is not strictly the case for this experiment.

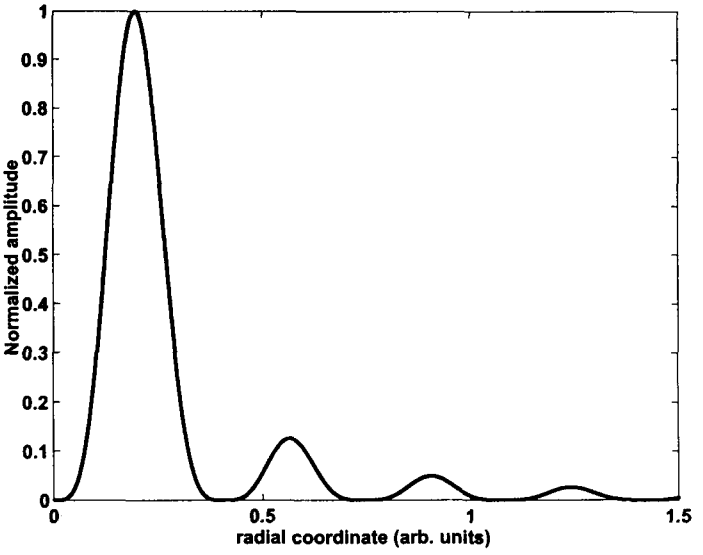

Figure 4.13. First order Bessel function of the first kind.

The distribution of the pattern in Fig. 4.12 has been characterized as a function of the radial coordinate. Pixel gray level values have been mapped to relative intensity in Fig.

4.14. The theoretical Bessel distribution has been superimposed in the plot. Note the general good agreement in the functional form of the intensity (crossed lines) except for a slight lateral shift of the zeroes and the unavoidable saturation of the CCD camera.

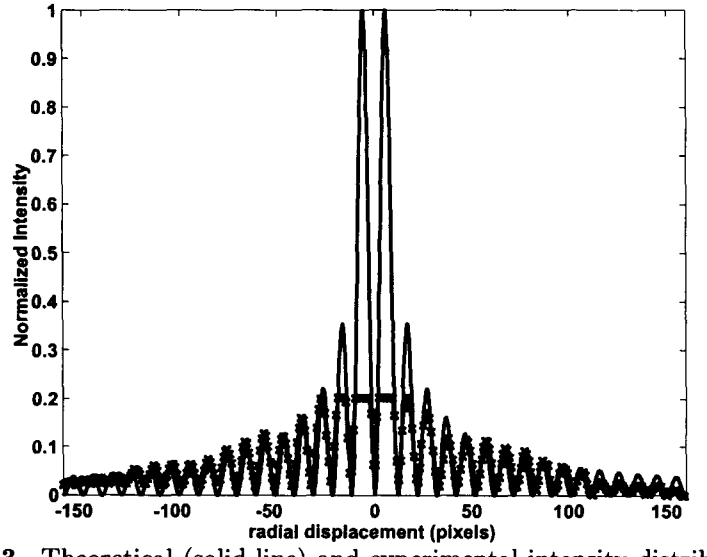

Figure 4.13. Theoretical (solid line) and experimental intensity distributions for a first order Bessel beam.

Note that even though the innermost levels reach only 20% of the theoretical maxima, the central minimum is considerably small in extent (3 pixels across). Also, it can be seen from Fig. 4.14 that the minima registered near the center is somewhat displaced above zero. This is explained by the effect that saturated pixels have over neighboring pixels despite low-light levels incident on the latter.

4.3.3 Invariance region measurements

The results so far show only intensity patterns of the wavefields at a fixed distance. This particular pattern is expected to be invariant as it propagates according to the theory outlined in chapter 2. In order to verify this, several photographs were taken at fixed intervals of 1 m from the output of the interferometer. The photographic sequence is shown in Figs. 4.15a to 4.15f for propagation distances $z = 1$ to 6 m and an output lens L_2 with focal length $f = 6$ in and radius $R = 2$ in. In this case, the invariance region is calculated as:

$$Z_{MAX} = f\frac{R}{a} = 7.74\ m \tag{4.16}$$

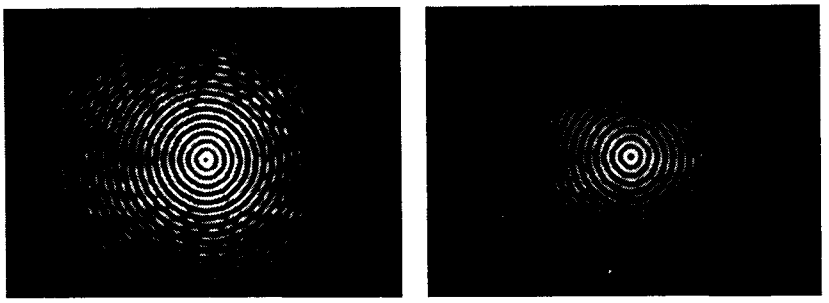

a. $z = 1$ m. **b.** $z = 2$ m.

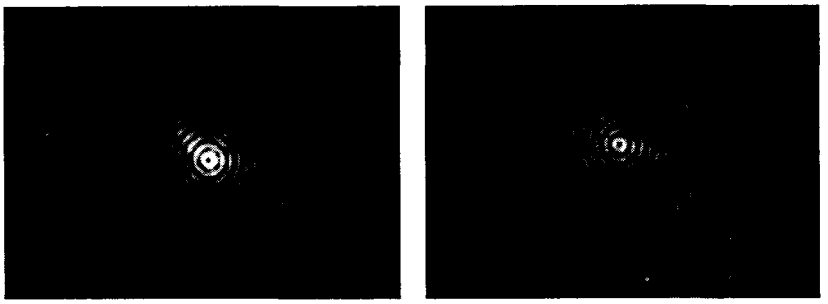

c. $z = 3$ m. **d.** $z = 4$ m.

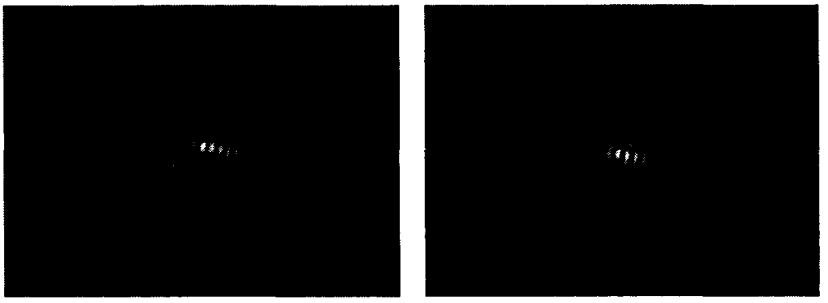

e. $z = 5$ m. **f.** $z = 6$ m.

Figures 4.15a-f. Photographic sequence of the evolution of a first order Bessel PIOF upon propagation.

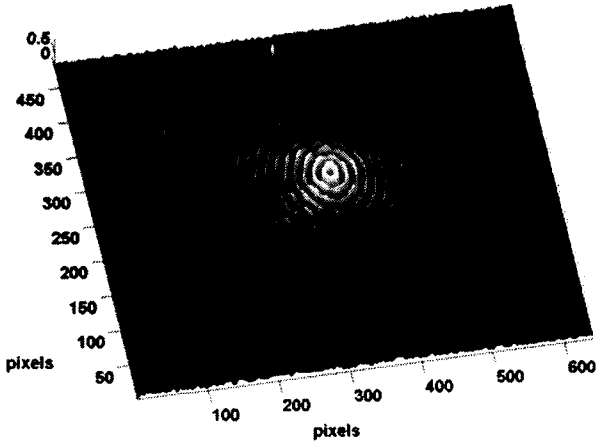

Figures 4.15g. Transverse intensity profile surface plot for $z = 2$ m.

It is evident from the photographs that the conical invariance region is degraded primarily in its surroundings as the propagation distance increases. Furthermore, the central region remains visible and relatively undistorted only to become less intense as it turns into the geometrical shadow as shown in Fig. 2.5. Clearly, the intensity pattern is severely altered at $\pm 45°$ after a few meters. These diagonal regions correspond to the overlapping of the boundaries of the circular components of the Bessel beam; a variation in intensity here becomes more evident after the conical waves propagate.

In view of Eq. 2.12, replacing the output lens for another lens of larger radius and focal length results in an increased invariance region. For lens parameters: $f = 15$ in and $R = 5$ in, one would now expect: $z_{MAX} = 48.38$ m. Because of physical limitations, it is difficult to attempt to measure invariance distances over 5 m, but certainly the quality of the observed beam will improve for a larger value of z_{MAX}. A different sequence with the new output lens is shown in Fig. 4.16. for propagation distances: $z = 0.25,\ 1.0,\ 2.0$ and 3.0 m.

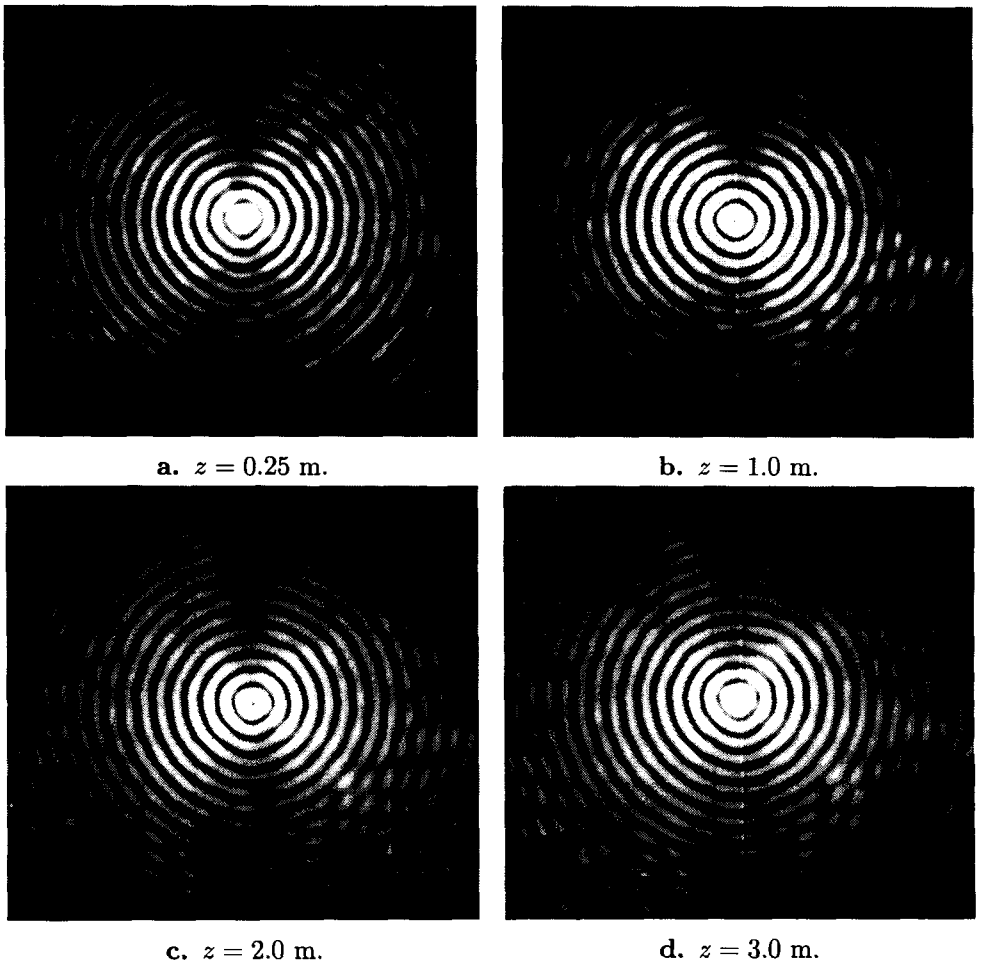

a. $z = 0.25$ m. **b.** $z = 1.0$ m.

c. $z = 2.0$ m. **d.** $z = 3.0$ m.

Figures 4.16a-f. Spatial evolution of a first order Bessel beam.

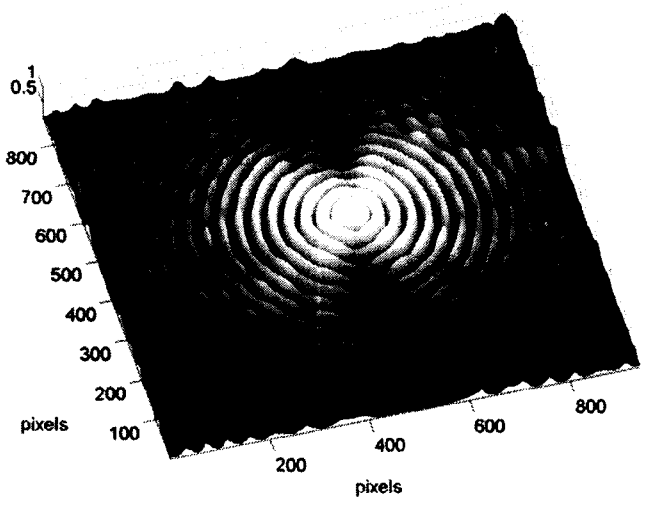

Figures 4.16g. Transverse intensity profile surface plot.

4.3.4 Observation of rotating wavefields

Thus far, only intensity distributions have been characterized. The phase distribution of the wavefield is nonetheless critical in the invariant and rotating characteristics of HOBBs. The intensity of a low-power visible wavefield is an easily observable physical quantity, either by direct or indirect methods. However, the phase of the field is a more subtle attribute and coherence observations require interferometric techniques as explained in chapter 3. Now that a reasonably good HOBB has been generated, the next step is the observation of the spatial rotation of its intensity pattern as the beam propagates. In order to achieve this, a plane wave was constructed with the same laser source by means of an additional beam splitter and it was set to interfere with the Bessel beam. An advantage in using the same source for interference is the null effect of the temporal coherence of the wave trains as long as the optical paths of the plane wavefront and those of each of the Bessel beam components are set to have the same length. The tolerance for optical path difference should be small compared to the coherence length for the laser source, which in this case was found to be about 49 cm. after the laser was stabilized. A path difference of the order of 1 in due to the breadboard grid spacing was thus rather acceptable.

With the purpose of obtaining a photographic sequence where the rotation of the intensity pattern could be observed, video captures of 4 to 7 seconds were performed while allowing the camera to move smoothly in the direction of propagation within the central part of the invariance region, for a number of rotations of the pattern. The capture was digitized by means of the frame grabber and the output was dumped as an Audio Video Interleaved (.avi) file. Raw data from single frames was extracted from the file and converted into bitmap (bmp) files. An example of such sequence in shown in Fig. 4.17. Note that the pattern is rotating clockwise from Fig. 4.17a to 4.17d. A reference feature that facilitates visualization of the rotation is the central minimum, note how it moves from the top vertical position to the middle left position in steps of

90 degrees.

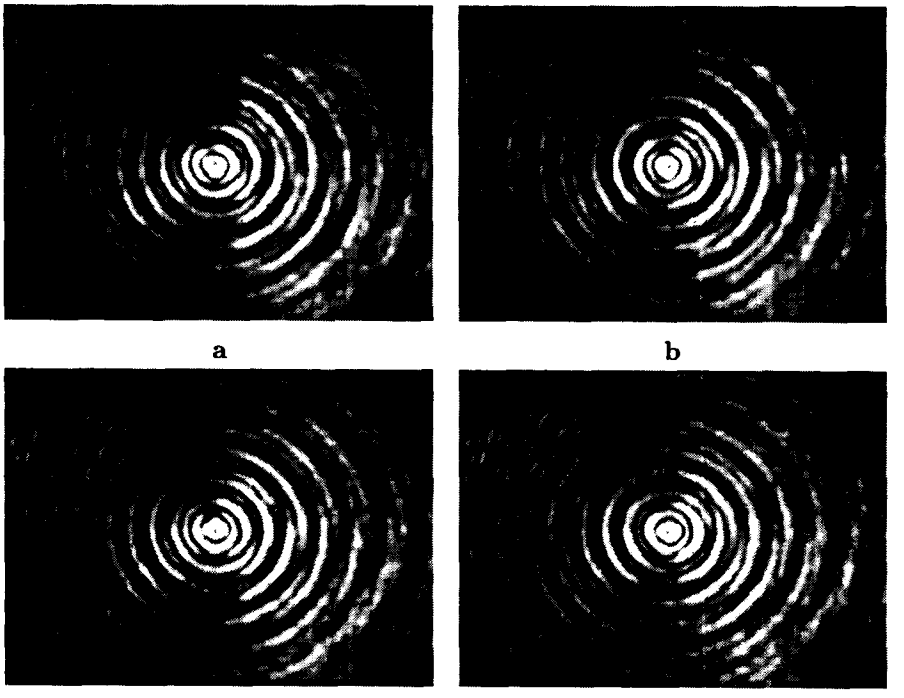

Figures 4.17a-d. Sequential video frames showing the evolution of a RW. Rotation is clockwise.

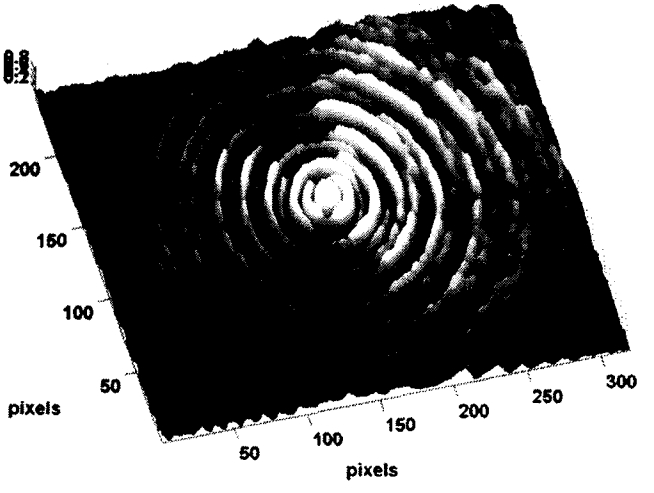

Figure 4.17e. Transverse intensity profile surface plot.

Note also that the phase shift between adjacent lobes is quite evident, particularly in the central area where bright circular sections are radially followed by narrow annular dark zones and dimmer lobes. Local maxima are observed in angularly opposite loci. For comparison purposes, the photographic sequence in Fig. 4.18a-f is a computer

simulation of the experiment.

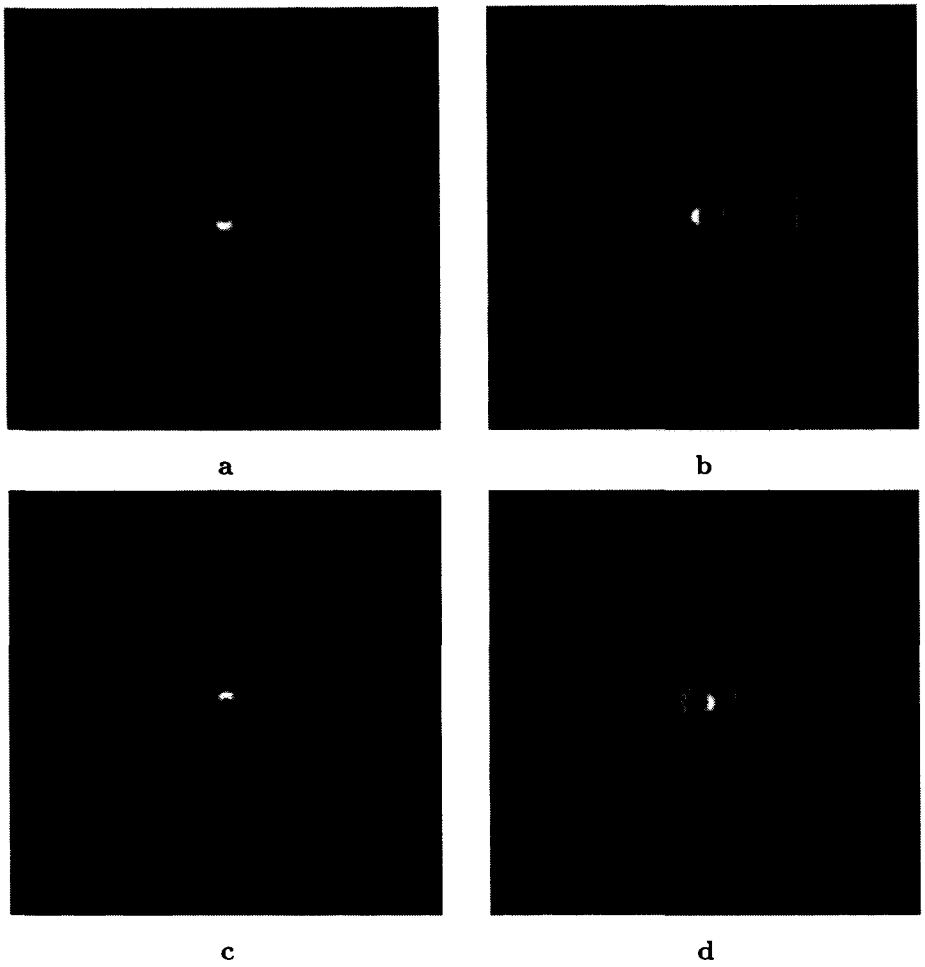

Figures 4.18a-d. Computer simulation of the evolution of the RW in Fig 4.17.

Even though the contrast in the sequence is acceptable, there is evidently a poor balance between the plane wave amplitude and the RMS value of the HOBB. This is due to the fact that the plane wave is not uniform in the planes of observation, this nonuniformity is mainly caused by the poor surface figure of the mirrors ($\lambda/4$) and beamsplitter ($\lambda/6$ max.) used to divide the wavefront in the interferometer. The experimental setup is thus very sensitive to slight random deformations of the plane wave.

Chapter 5

Conclusions

This chapter briefly outlines the achievements of this work and discusses the technical problems that arose during experimental activities. Further work is also suggested as an extension to the results presented herein.

5.1 Milestones

In this work we have successfully produced a high order Bessel beam by adding its even and odd angular components. The approach used for this purpose was the construction of each component separately and the further interference of both by means of a Mach-Zehnder arrangement. In this manner, it has been shown that a HOBB can be constructed in a relatively simple and inexpensive way. An additional advantage of the arrangement is the use of binary half-wave phase changes for the transmission slits that generate the Bessel components.

Several techniques were attempted to develop a local phase retardation method with low deformation of the wave front. Materials used in this regard include plastic retarders, quartz, mica and silica.

Perhaps the most important achievement of the present work is the reliable generation of a zeroth order Bessel beam and the practical demonstration that phase modulation can be performed with only a few microscopic manipulation tools. An exceptional feature of the experimental techniques used here is its low cost when compared to using state of the art electron beam lithography or deposition techniques to produce an annular slit.

Successful generation of a first order Bessel beam was also achieved; the interferometric setup proposed for this purpose proved to be an effective though cumbersome method, in particular because of the fabrication and manipulation of the transmission gratings. The resulting beam was characterized and good agreement with a Bessel transverse intensity distribution was found.

Rotation of the first order Bessel beam was achieved and its gradual phase distribution observed in single frames captured from a video sequence. The alternate radial phase shift between adjacent lobes was also observed using this procedure. The results

obtained herein have been presented at the annual meeting of the International Society for Optical Engineering (SPIE) 2003 [42].

Numerous results were presented in photographic form, however, a considerable amount of additional work can be done using the experimental setup by modifying the transmission plates thus altering their geometrical and optical parameters. Necessarily, a more robust setup must be implemented in order to make detailed observations of physical properties such as momentum and energy flux within the context of the application of HOBBs to atomic traps. Finally, in order to attain repeatability of he experiment suitable for accurate measurements, finer mechanical subsystems are imprescindible.

5.2 Difficulties

To the eye of the unexperienced, overestimation of the available resources and their usage might result in unnecessarily laborious and time-consuming tasks that could otherwise be avoided. This was the case regarding the available equipment for the construction of the interferometer.

Most of the problems in obtaining acceptable results from the experiments described above arose from financial limitations of the project. Clearly, an interferometric experiment requires the use of high-quality optics, particularly regarding the surface figures of diffractive and reflective elements, such as mirrors and lenses. Additionally, the procedure used to record intensity patterns of rotating wavefields described in sect. 4.3.4 is not the most suitable one given that the manual motion of the camera induced unwanted displacement of several optical elements in the setup. The use of an automated precision translation stage would be highly convenient.

Other difficulties arose in the construction process of the transmission plates. Manual cutting, placement, and bonding of small plastic parts proved to be the most time-consuming task in the entire development of the experiment. The fact that once made, the plates were in general impossible to modify added complexity and increased preparation time for every trial. The construction of the plates is quite simple in principle, given that the proper tools for micromanipulation are available.

Interference of HOBBs and spherical wavefronts require of proper control of the reference waveforms. Due to the low surface figure of the reflective optics, it was difficult to achieve an extended wavefront with reasonable accuracy.

Finally, as the experiment requires a considerably powerful light source, a high-voltage power supply was refurbished for the purpose. This was perhaps the most temperamental piece of equipment within the setup and the cause for the most important delays in between trials.

5.3 Forthcoming experimentation

In order to obtain a more accurate picture of the intensity distribution of the HOBBs and RWs involved in the experiments, and due to the broad dynamic range of these,

it would be more convenient to use laser profiling hardware instead of photographic techniques. Evidently, the truncation of high brightness values would be somewhat diminished in this manner.

The construction of reliable spherical wavefronts will allow for the observation of more complex phenomena, such as the nonuniform rotation of the wavefields. For this purpose, lower-tolerance surface figures should be used ($\lambda/10$ at least) in reflective surfaces.

Additionally, an alternate method for the generation of the angular even and odd Bessel components should be used, so as to produce Bessel beams of order $m \gg 1$. In this respect, spatial light modulators are most promising but expensive devices.

5.4 Future work

Recently, a new technique for the generation of binary Fourier holograms has been developed [43]. The technique makes use of commercially available optical media (CD-R) and writer to map the interferogram onto the surface of the compact disc. Because of its high spatial resolution, the usage of this media for transmission plates can result in improved beam quality. Also, using transparent diffractive or reflective methods to generate the HOBBs can be more efficient than, specially in the case of the annular slit, where most of the incident power is lost.

The use of SLMs to generate the desired wavefronts could be as well advantageous, but its feasibility is limited by their low diffraction efficiency and high cost.

Bibliography

[1] M.S. Longair, *High Energy Atrophysics*, vol. 2. Stars, the Galaxy and the interstellar medium, Cambridge University press, Cambridge, second edition, 1997.

[2] J.J. Micely Jr. J. Durnin and J.H. Eberly, "Diffraction-free beams", *Phys. Rev. Lett.*, vol. 58, no. 15, pp. 1499–1501, April 1987.

[3] J. Durnin, "Exact solutions for non-diffracting beams. i. the scalar theory", *J. Opt. Soc. Am.*, vol. 4, no. 4, pp. 651–654, 1987.

[4] E.T. Whittaker and G.N. Watson, *A Course of Modern Analysis*, Cambridge University Press, Westford, Mass., 4th edition, 1927.

[5] A. Vasara J. Turunen and A.T Friberg, "Propagation invariance and self-imaging in variable-coherence optics", *J. Opt. Soc. Am. A*, vol. 8, no. 2, pp. 282–289, 1991.

[6] J. Wagner Z. Bouchal, "Self-reconstruction effect in free propagation of wavefield", *Opt. Commun.*, , no. 179, pp. 299–307, 2000.

[7] M. D. Iturbe-Castillo J.C. Gutiérrez-Vega and S. Chávez-Cerda, "Alternative formulation for invariant optical fields: Mathieu beams", *Opt. Lett.*, vol. 25, no. 20, pp. 1493–1495, 2000.

[8] T.A. Wiggins R.M. Herman, "Production and uses of diffractionless beams", *J. Opt. Soc. Am. A*, vol. 8, no. 6, pp. 932–942, 1991.

[9] D. Milam Y. Song and W. T. Hill III, "Long, narrow all-light atom guide", *Opt. Lett.*, vol. 24, no. 24, pp. 1805–1807, 1999.

[10] J.H. McLeod, "The axicon: A new type of optical element", *J. Opt. Soc. Am.*, vol. 44, no. 8, pp. 592–597, 1954.

[11] J.C. Gutiérrez-Vega M. Bandrés and S. Chávez-Cerda, "Parabolic nondiffracting wavefield", *Opt. Lett.*, vol. (to be published), 2003.

[12] W. Sibbett J. Arlt, V. Garcés-Chávez and K. Dholakia, "Optical micromanipulation using a bessel light beam", *Opt. Commun.*, , no. 197, pp. 239–245, 2001.

[13] V. Garcés-Chávez D. McGloin and K. Dholakia, "Interfering bessel beams for optical micromanipulation", *Opt. Lett.*, vol. 28, no. 8, pp. 657–659, 2003.

[14] H. Melville W. Sibbet D. McGloin, G. C. Spalding and K. Dholakia, "Three-dimensional arrays of optical bottle beams", *Opt. Commun.*, vol. 225, pp. 215–222, 2003.

[15] J.C. Gutiérrez-Vega, *Formal Analysis of the Propagation of Invariant Optical Fields with Elliptic Symmetres*, PhD thesis, INAOE, 2000.

[16] H. Kogelnik and T. Li, "Laser beams and resonators", *Proc. IEEE*, vol. 54, pp. 1312–1392, 1966.

[17] M. Born and E. Wolf, *Principles of Optics*, Cambridge University Press, Cambridge, 7th edition, 1999.

[18] J.J. Miceli J. Durnin and J.H. Eberly, "Comparison of bessel and gaussian beams", *Opt. Lett.*, vol. 13, no. 2, pp. 79–80, 1988.

[19] A.A. Friesem N. Davidson and E. Hasman, "Diffractive elements for annular laser beam transformation", *Appl. Phys. Lett.*, vol. 61, no. 4, pp. 381–383, 1992.

[20] J. Arlt C.A. McQueen and K. Dholakia, "An experiment to study a "nondiffracting" light beam", *Am. J. Phys.*, vol. 67, no. 10, pp. 912–915, 1999.

[21] G.S. McDonald S. Chávez-Cerda and G.H.C New, "Non-diffracting beams: Travelling, standing, rotating, and spiral waves", *Opt. Commun.*, vol. 123, pp. 225–233, 1996.

[22] J. C. Gutiérrez-Vega S. Chávez-Cerda and R. Rodríguez-Masegosa, "Focusing evolution of generalized propagation invariant optical fields", *J. Opt. A: Pure Appl. Opt.*, , no. 5, pp. 276–282, 2003.

[23] J. Ojeda-Castañeda A.W. Lohmann and N. Streibl, "Spatial periodicities in coherent and partially coherent fields", *Opt. Acta*, vol. 40, no. 9, pp. 1259–1266, 1983.

[24] G.S. Agarwal M.W. Kowarz, "Bessel-beam representation for partially coherent fields", *J. Opt. Soc. Am. A*, vol. 12, no. 6, pp. 1324–1330, 1995.

[25] J. Shamir R. Piestun, "Generalized propagation-invariant wave fields", *J. Opt. Soc. Am. A*, vol. 15, no. 12, pp. 3039–3044, 1998.

[26] A. E. Siegman, *Lasers*, University Science Books, Sausalito, CA, 1986.

[27] E. Hecht, *Optics*, Addison Wesley, third edition, 1998.

[28] K. Dholakia J. Arlt, "Generation of high-order bessel beams by use of an axicon", *Opt. Commun.*, , no. 177, pp. 297–301, 2000.

[29] J.W. Goodman, *Principles of Fourier Optics*, Mc-Graw Hill, New York, 2nd edition, 1996.

[30] P. Vahimaa-J. Turunen P. Pääkkönen, J. Tervo and F. Gori, "General vectorial decomposition of electromagnetic fields with application to propagation-invariant and rotating fields", *Opt. Express*, vol. 10, no. 18, pp. 949–959, 2002.

[31] V. Kuittinen-J. Turunen P. Vahimaa, P. Kettunen and A.T. Friberg, "Electromagnetic analysis of nonparaxial bessel beams generated by diffractive axicons", *J. Opt. Soc. Am. A*, vol. 14, pp. 1817–1824, 1997.

[32] M. Ciofini A. Lapucci, "Polarization state modifcations in the propagation of high azimuthal order annular beams", *Opt. Express*, vol. 9, no. 12, pp. 603–609, 2001.

[33] G. Indebetouw, "Nondiffracting optical fields: Some remarks on their analysis and synthesis", *J. Opt. Soc. Am. A*, vol. 6, no. 1, pp. 150–152, 1989.

[34] M.A. Meneses Nava G. Ramírez S. Chávez-Cerda, E. Tepichín and J.M. Hickman, "Experimental observation of interfering bessel beams", *Opt. Exp.*, vol. 3, no. 13, pp. 524–529, December 1998.

[35] A.T. Friberg J. Turunen, "Self-imaging and propagation-invariance in electromagnetic fields", *Pure Appl. Opt.*, , no. 2, pp. 51–60, 1993.

[36] J. Turunen J. Tervo, "Rotating scale-invariant electromagnetic fields", *Opt. Express*, vol. 9, no. 1, pp. 9–15, 2001.

[37] M. Honkanen M. Kuittinen J. Turunen S.N. Khonina V.V. Kotlyar V. A. Soifer P. Pääkkönen, J. Lautanen and A.T. Friberg, "Rotating optical fields: Experimental demonstration with diffractive optics", *J. Mod. Opt.*, vol. 45, no. 11, pp. 2355–2369, 1998.

[38] Y.Y. Schechner R. Piestun and J. Shamir, "Propagation-invariant wave fields with finite energy", *J. Opt. Soc. Am. A*, vol. 17, no. 2, pp. 294–303, 2000.

[39] V.A. Soifer M. Honkanen J. Lautanen S.N. Khonina, V.V. Kotlyar and J. Turunen, "Generation of rotating gauss-laguerre mode with binary-phase diffractive optics", *J. Mod. Opt*, vol. 42, no. 2, pp. 227–238, 1999.

[40] N. Davidson G. Machavariani and E. Hasman, "Efficient conversion of a gaussian beam to a high purity helical beam", *Opt. Commun.*, , no. 209, pp. 265–271, 2002.

[41] R. Kuhn J. Arlt and K. Dholakia, "Spatial transformation of laguerre-gaussian laser modes", *J. Mod. Opt.*, vol. 48, no. 5, pp. 783–787, 2001.

[42] SPIE, annual meeting, *High-Order Bessel Beam and Rotating Wavefields Using a Mach-Zehnder Interferometer*, San Diego, USA, 2003.

[43] P. Mash A. Cable and T. Wilkinson, "Production of computer-generated holograms on recordable compact disk media using a compact disk writer", *Opt. Eng.*, vol. 9, no. 42, pp. 2514–2520, 2003.